# Absorption-line strengths of 18 late-type spiral galaxies observed with SAURON

Ganda, Katia; Peletier, Reynier F.; McDermid, Richard M.; Falcon-Barroso, Jesus; de Zeeuw, P. T.; Bacon, Roland; Cappellari, Michele; Davies, Roger L.; Emsellem, Eric; Krajnovic, Davor

*Published in:*
Monthly Notices of the Royal Astronomical Society

*DOI:*
10.1111/j.1365-2966.2007.12121.x



*Publication date:*
2007

Mon. Not. R. Astron. Soc. **380,** 506–540 (2007) doi:10.1111/j.1365-2966.2007.12121.x

# Absorption-line strengths of 18 late-type spiral galaxies observed with SAURON

Katia Ganda,[1⋆] Reynier F. Peletier,[1] Richard M. McDermid,[2] Jesús Falcón-Barroso,[2,3] P. T. de Zeeuw,[2] Roland Bacon,[4] Michele Cappellari,[5] Roger L. Davies,[5] Eric Emsellem,[4] Davor Krajnović,[5] Harald Kuntschner,[6] Marc Sarzi[5,7] and Glenn van de Ven[2,8]†

[1]*Kapteyn Astronomical Institute, University of Groningen, PO Box 800, 9700 AV Groningen, the Netherlands*
[2]*Sterrewacht Leiden, University of Leiden, Niels Bohrweg 2, 2333 CA Leiden, the Netherlands*
[3]*European Space Agency/ESTEC, Keplerlaan 1, 2200 AG Noordwijk, the Netherlands*
[4]*CRAL, Observatoire de Lyon, CNRS, UMR 5574, ENS de Lyon, Université de Lyon 1, 9 avenue Charles André, F-69230 Saint Genis Laval Cedex, France*
[5]*Sub-Department of Astrophysics, University of Oxford, Denys Wilkinson Building, Keble Road, Oxford OX1 3RH*
[6]*Space Telescope European Coordinating Facility, European Southern Observatory, Karl-Schwarzschild-Str. 2, 85748 Garching, Germany*
[7]*Centre for Astrophysics Research, University of Hertfordshire, Hatfield, Hertfordshire AL10 9AB*
[8]*Institute for Advanced Study, Einstein Drive, Princeton, NJ 08540, USA*

Accepted 2007 June 17. Received 2007 June 13; in original form 2007 March 12

**ABSTRACT**

We present absorption line strength maps for a sample of 18 Sb–Sd galaxies observed using the integral-field spectrograph SAURON operating at the William Herschel Telescope on La Palma, as part of a project devoted to the investigation of the kinematics and stellar populations of late-type spirals, a relatively unexplored field. The SAURON spectral range allows the measurement of the Lick/IDS indices H$\beta$, Fe5015 and Mg*b*, which can be used to estimate the stellar population parameters. We present here the two-dimensional line strength maps for each galaxy. From the maps, we learn that late-type spiral galaxies tend to have high H$\beta$ and low Fe5015 and Mg*b* values, and that the H$\beta$ index has often a positive gradient over the field, while the metal indices peak in the central region.

We investigate the relations between the central line strength indices and their correlations with morphological type and central velocity dispersion, and compare the observed behaviour with that for ellipticals, lenticulars and early-type spirals from the SAURON survey. We find that our galaxies lie below the Mg$-\sigma$ relation determined for elliptical galaxies and that the indices show a clear trend with morphological type.

From the line strength maps we calculate age, metallicity and abundance ratio maps via a comparison with model predictions; we discuss the results from a one-SSP (single stellar population) approach and from a two-SSP approach, considering the galaxy as a superposition of an old ($\approx$13 Gyr) and a younger (age $\leqslant$5 Gyr) population. We confirm that late-type galaxies are generally younger and more metal-poor than ellipticals and have abundance ratios closer to solar values. We also explore a continuous star formation scenario, and try to recover the star formation history using the evolutionary models of Bruzual & Charlot, assuming constant or exponentially declining star formation rate. In this last case, fixing the galaxy age to 10 Gyr, we find a correlation between the e-folding time-scale $\tau$ of the starburst and the central velocity dispersion, in the sense that more massive galaxies tend to have shorter $\tau$, suggesting that the star formation happened long ago and has now basically ended, while for smaller objects with larger values of $\tau$ it is still active now.

**Key words:** galaxies: bulges – galaxies: evolution – galaxies: formation – galaxies: kinematics and dynamics – galaxies: spiral – galaxies: structure.

⋆E-mail: katia@astro.rug.nl
†Hubble Fellow.

## 1 INTRODUCTION

Over the last few decades, stellar population synthesis has become one of the most popular and powerful techniques to study the formation and evolution histories of galaxies too distant to be resolved into individual stars. In particular, the measurement of absorption line strengths combined with stellar population models has been used to investigate the luminosity-weighted age, metallicity and abundance ratios in integrated stellar populations. Extensive work has been carried out on stellar populations in early-type galaxies, mainly using long-slit spectra (see e.g. Carollo, Danziger & Buson 1993; Davies, Sadler & Peletier 1993; Fisher, Franx & Illingworth 1995, 1996; Longhetti et al. 1998; Jørgensen 1999; Kuntschner 2000; Sánchez-Blázquez et al. 2007) and recently also integral-field spectroscopy (Kuntschner et al. 2006, hereafter Paper VI; McDermid et al. 2006, hereafter Paper VIII). The main advantage brought by the integral-field observations is that one can obtain two-dimensional maps and easily identify extended structures. In particular, the two-dimensional coverage gives the possibility to straightforwardly connect the stellar populations with the kinematical structures and therefore represents a powerful tool towards a comprehensive understanding of the structure of the galaxy.

Some literature is also available on absorption line strengths in early-type spiral galaxies, mainly S0 and Sa galaxies; (see e.g. Idiart, de Freitas Pacheco & Costa 1996; Jablonka, Martin & Arimoto 1996; Proctor & Sansom 2002; Afanasiev & Sil'chenko 2005; Peletier et al. 2007, hereafter Paper XI). In particular, Paper XI presents two-dimensional absorption line strength maps of 24 spiral galaxies, mostly of type Sa, observed with the integral-field spectrograph SAURON (Bacon et al. 2001, hereafter Paper I); these reveal young populations in Sa galaxies, possibly formed in ministarbursts in structures such as nuclear discs, circular star-forming rings and bars. These ministarbursts generate a large scatter in index–index diagrams, larger than observed for elliptical galaxies. As a consequence, there is a large range in luminosity-weighted ages. Different star formation modes – starbursts or quiescent – are also reflected in the wide range observed in the abundance ratios. All the galaxies of Paper XI lie on or below the Mg$b$–$\sigma$ relation for ellipticals determined by Jørgensen, Franx & Kjærgaard (1996). The authors argue that, if one considers that relation as valid for old galaxies, then the early-type spirals present a scatter in age, with the biggest scatter for the smallest velocity dispersions.

Spiral galaxies towards the end of the Hubble sequence are, on the other hand, still poorly studied objects, due to the difficulty of obtaining reliable measurements in these low surface brightness objects, full of dust and star-forming regions, whose spectra can be dramatically contaminated by emission lines. In particular, the study of their stellar populations is extremely complicated. An approach based on broad-band colours is basically invalidated by the huge amount of dust, which is very difficult to take into account, especially when working with data from ground-based telescopes. A spectroscopic approach, relying, for example, on stellar absorption strength indices, has instead to deal with the almost ubiquitous presence of gas with consequent emission, which makes it necessary to accurately remove the emission lines from the spectra before performing any population analysis. Only in the last decade several *HST*-based imaging surveys have targeted these late-type galaxies. Particularly relevant are the papers by Carollo et al. (1997), Carollo & Stiavelli (1998), Carollo, Stiavelli & Mack (1998), Carollo (1999), Carollo et al. (2002), Böker et al. (2002), Laine et al. (2002), where the authors reveal the presence of a variety of structures in the inner regions, such as bulges, nuclear star clusters, stellar discs, small bars, double bars and star-forming rings whose formation and evolutionary pattern are not properly understood yet. Carollo et al. (2007) also performed a population analysis on nine late-type spiral galaxies (types between Sa and Sc) on the basis of *HST* ACS and NICMOS optical and near-infrared (NIR) colours. The high spatial resolution of their space-based data allowed them to mask dust features and measure the properties of the stellar populations from the colours; this method, together with the high spatial resolution provided by *HST*, produced results that do not suffer much from the effects of dust; only a smooth dust distribution would not be detected. From their analysis, they found a large range in the colour properties of bulges in late-type spirals, reflecting a large range in their stellar population properties. From a comparison with population models, they concluded that in about half of their bulges the bulk of the stellar mass formed at early epochs (more than 50 per cent of their mass was formed more than 9 Gyr ago), and that in the other half a non-negligible fraction of the stellar mass (up to 25 per cent) was formed recently, in the last $\approx$3 Gyr.

Until now, only little spectroscopic counterpart for the quoted imaging was available, due to the mentioned observational difficulties. The published work (Zaritsky, Kennicutt & Huchra 1994; Böker et al. 2001; Matthews & Gallagher 2002; Rossa et al. 2003; Walcher et al. 2005) mainly refers to the emission line properties, to the characteristics of the H II regions or to the nature of the innermost component. In particular, no study has addressed yet in a systematic way the stellar populations of late-type spiral galaxies with a two-dimensional coverage. Existing studies on abundances concern topics such as elemental abundances in H II regions and the distribution of oxygen within discs (Zaritsky et al. 1994), not properties inferred from the integrated stellar absorption spectrum. As for the absorption line properties, there is ongoing work by MacArthur, Gonzalez & Courteau (2007), who analyse long-slit spectra (Gemini – GMOS) of eight spiral galaxies of type between Sa and Scd on a wide spectral range, measuring many absorption indices out to 1–2 disc scalelengths. Also, Moorthy & Holtzman (2006) presented line strengths in the bulges and inner discs of 38 galaxies of morphological type between S0 and Sc for which they acquired long-slit spectra on a broad spectral range including Balmer lines, Mg and Fe features. They concluded that the central regions of bulges span a wide range both in single stellar population (SSP) metallicity and age, confirming the results of Carollo et al. (2007). They also found that luminosity-weighted metallicities and abundance ratios are sensitive to the value of the central velocity dispersion and of the maximum disc rotational velocity, and that red bulges (defined as those with $B - K > 4$) of all types are similar to luminous ellipticals and obey the same scaling relations; for the blue bulges ($B - K < 4$) they observed instead some differences. They also addressed the radial variations of the population parameters; in most cases, they measured negative metallicity gradients with increasing radius, in the bulge-dominated region; positive gradients in age were found only in barred galaxies.

As mentioned, there is still a lack of work on populations in late-type spirals on a full two-dimensional field: we therefore started a project on a sample of 18 late-type spiral galaxies, with the purpose of investigating the nature of their inner regions, addressing the bulge and disc formation and evolution, the interconnection between stellar and gaseous components and the star formation history. Given the high complexity in the inner regions of these objects,

integral-field spectroscopy has to be preferred with respect to long slit, providing a full picture of the kinematics and populations on a two-dimensional field of view (FoV). We observed our 18 late-type spiral galaxies using SAURON, an integral-field spectrograph that was built for a representative census of ellipticals, lenticulars and early-type spiral galaxies, to which in the rest of this paper we will refer as 'the SAURON survey'. Our project can be regarded as an extension of the SAURON survey towards later type objects. First results based on our data are presented by Ganda et al. (2006) and focus on the stellar and gas kinematical maps. The main findings of that paper are that in many cases the stellar kinematics suggests the presence of a cold inner region, as visible from a central drop in the velocity dispersion, detected in about one-third of the sample; that the ionized gas is almost ubiquitous and often presents more irregularities in its kinematics than the stellar component; and that the line ratio [O III]/H$\beta$ assumes often low values over most of the field, possible indication for widespread star formation, in contrast to early-type galaxies.

As a following step in our project, we subtracted the emission lines from our SAURON spectra, measured as explained in Ganda et al. (2006), and on the emission-cleaned spectra derived absorption line strength indices in the Lick/IDS system (Faber et al. 1985; Gorgas et al. 1993; Worthey et al. 1994), which allows an easier comparison with existing data and with other classes of objects. Here we present and analyse the absorption line strength maps. The data and maps presented in this paper will be made available via the SAURON WEB page http://www.strw.leidenuniv.nl/sauron/.

The paper is structured as follows. Section 2 briefly describes the sample selection, observations and data reduction. Section 3 reviews the analysis methods. In Section 4 we present the line strength maps for all the galaxies in our sample. In Section 5 we investigate the correlations between different indices and between indices and other galactic parameters, such as the morphological type and the central velocity dispersion, mainly focusing on the central values. In Section 6 we present our estimates for the ages and metallicities, obtained by comparison of our observed line strength indices with model predictions; we also explore the star formation history and give estimates for the time-scale $\tau$, in an exponentially declining SFR scenario. Section 7 summarizes the main results. In Appendix A we deal with the radial variations of the indices and the stellar population parameters, presenting azimuthally averaged radial profiles. Appendix B shortly describes the individual galaxies and their peculiarities, giving a brief summary of relevant literature information. For more literature reviews on these objects, we suggest the reader to check section 6.4 in Ganda et al. (2006).

## 2 SAMPLE SELECTION, OBSERVATIONS AND DATA REDUCTION

The galaxies were optically selected ($B_T < 12.5$, according to the values given in de Vaucouleurs et al. 1991, hereafter RC3) with *HST* imaging available from WFPC2 and/or NICMOS. Their morphological type ranges between Sb and Sd, following the classification given in NASA/IPAC Extragalactic Database (NED)[1] (from the RC3). Galaxies in close interaction and Seyferts were discarded. The resulting sample contains 18 nearby galaxies, whose main properties are listed and illustrated, respectively, in table 1 and fig. 1 in Ganda et al. (2006). The NGC numbers and some characteristics are reported also in the tables in the present paper. Observations of the 18 sample galaxies were carried out during six nights in 2004 January, using the integral-field spectrograph SAURON attached to the 4.2-m William Herschel Telescope. The exposure details are listed in table 2 in Ganda et al. (2006).

We used the low spatial resolution mode of SAURON, giving an FoV of 33 $\times$ 41 arcsec$^2$. The spatial sampling of individual exposures is determined by an array of 0.94 $\times$ 0.94-arcsec$^2$ square lenses. This produces 1431 spectra per pointing over the SAURON FoV; another 146 lenses sample a region 1.9 arcmin away from the main field in order to measure simultaneously the sky background. SAURON delivers a spectral resolution of 4.2 Å FWHM, and its maximum spectral coverage is 4800–5380 Å; the wavelength interval common to all lenses is the narrow spectral range 4825–5275 Å (1.1 Å pixel$^{-1}$). This wavelength range includes a number of important stellar absorption lines (e.g. H$\beta$, Fe5015, Mg*b*), and potential emission lines as well (H$\beta$, [O III], [N I]). For a more exhaustive description of the instrument, see Paper I.

Data reduction was carried out using the dedicated software XSAURON developed at Centre de Recherche Astronomique de Lyon (CRAL). For details on the data reduction we refer the reader to Paper I and Ganda et al. (2006). For an explanation of the spectrophotometric calibration we recommend the reader to study Paper VI, in particular its section 3.1.

## 3 ANALYSIS AND METHODS

The fully reduced and calibrated spectra were first spatially binned using a Voronoi tessellation (Cappellari & Copin 2003) in order to reach a minimum signal-to-noise ratio (S/N) of $\approx$60 per spectral resolution element per bin. The kinematics of stars and gas were then extracted from the binned spectra via the pixel-fitting methods, extensively described in Cappellari & Emsellem (2004), Emsellem et al. (2004, hereafter Paper III) and Sarzi et al. (2006, hereafter Paper V), that we already applied to calculate the kinematical maps shown in Ganda et al. (2006). The spectra were fitted using the SSP models from Vazdekis (1999). We selected a library of 48 models evenly sampling a wide range in both age and metallicity ($0.50 \leqslant$ age $\leqslant 17.78$ Gyr, $-1.68 \leqslant$ [Fe/H] $\leqslant +0.20$). We used this SSP library and additional Gaussian templates reproducing the emission lines to fit the observed spectra, separating the emission lines from the underlying absorption line spectrum (see Paper V, for details on the procedure). We note that for our objects this separation is crucial if we want to measure absorption strengths, since in spiral galaxies the gas is almost ubiquitous and emission in several cases dominates the spectrum, filling in completely the absorption features, as shown, for example, in the cases of some central aperture spectra in the top row of Fig. 1 (black lines); in the same figure we overplot the best fit to the spectra obtained with our method (red lines) and the emission-removed spectra (blue lines), illustrating the reliability of the applied gas-cleaning procedure. The bottom row of Fig. 1 presents similar plots for bins located $\approx$10 arcsec from the galaxy's centre, showing that our fits and emission correction are reliable also outside the central region, given the fact that a minimum S/N of 60 is guaranteed by the spatial binning. The reader can find more examples of this in fig. 1 in Paper V, fig. 3 in Ganda et al. (2006) and fig. 3 in Falcón-Barroso et al. (2006), hereafter Paper VII.

[1] http://nedwww.ipac.caltech.edu.

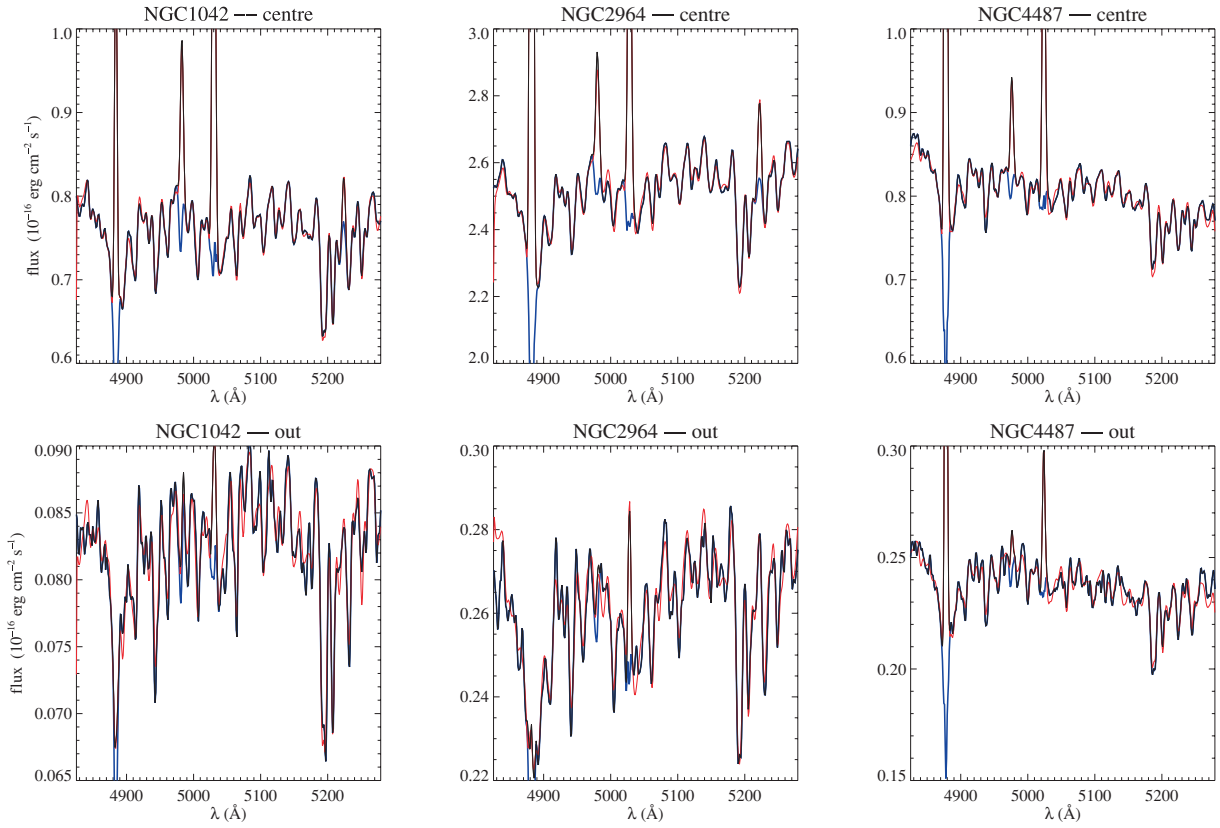


**Figure 1.** Top row: central aperture spectra of some representative galaxies in our sample: from left- to right-hand side, we plot NGC 1042, 2964 and 4487. Along the vertical axis, the flux is in units of $10^{-16}$ erg cm$^{-2}$ s$^{-1}$. The black lines – hardly distinguishable from the other ones – represent the observed spectra; the red ones the best fit and the blue ones the spectra after emission removal. Bottom row: as in the top row, but for bins located ≈10 arcsec away from the galaxy's centre.

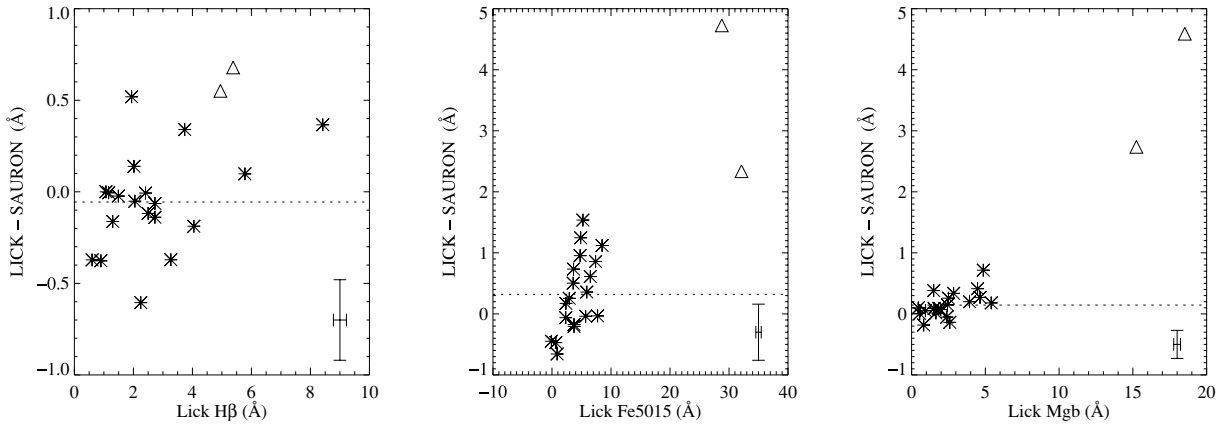


**Figure 2.** Differences between the Lick/IDS and our measurements for the 21 stars in common, for the three indices. For two stars (HD18191 and HD114961, spectral type, respectively, M6III and M7III) our measurements of the metal indices differ dramatically from the Lick/IDS measurements; therefore we excluded them from the determination of the offsets and plotted them with a different symbol (open triangles). The overplotted dashed line shows the adopted offset, derived by a biweight estimator. In the bottom right-hand corner we place a typical error bar.

We also note that in two cases (viz. NGC 2964 and 4102) we detected regions of activity (see Ganda et al. 2006, for a description), where the spectra are characterized by double-peaked emission lines due to the presence of multiple velocity components in the gas, because of the presence of a jet. In those regions our method of fitting the lines with single Gaussians fails to reproduce accurately the line profile, but since this is limited to only a few spectra, we did not modify the method. In any case, this does not have any impact on our following analysis, since the double-peaked emission lines do not contaminate the spectra defining the central aperture (see Section 5) on which most of this study is focused on.

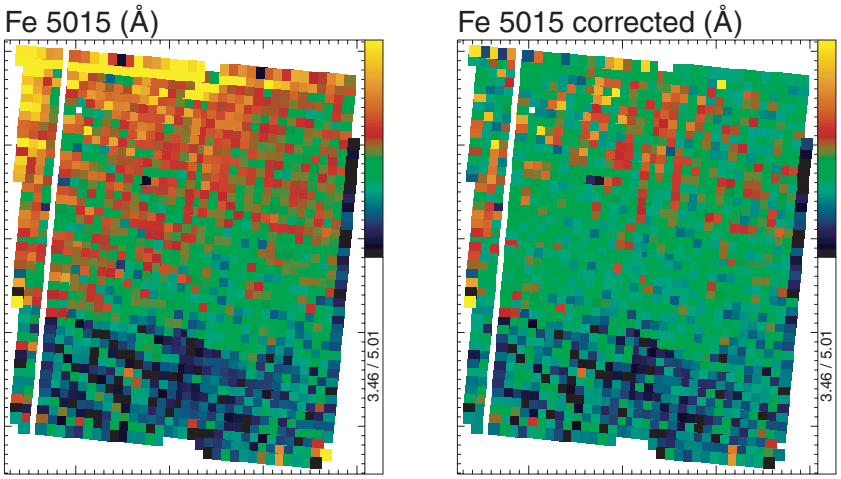


**Figure 3.** Maps of the Fe5015 index for the twilight frame, before and after correction, in Å. The two maps are plotted with the same cuts, indicated on their side, together with the colour bar. In the corrected frame, the spatial gradient is largely removed.

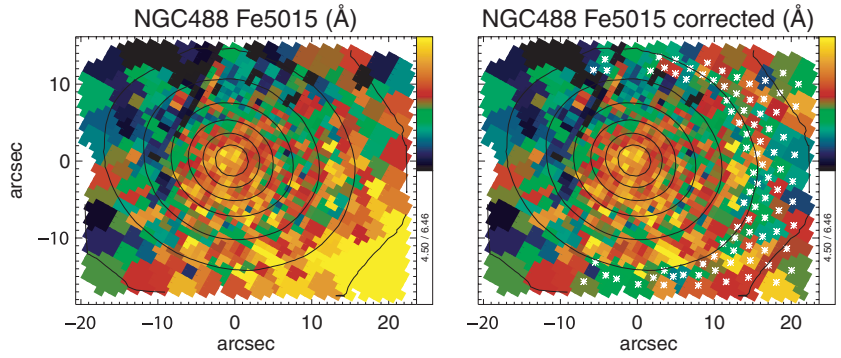


**Figure 4.** Maps of the Fe5015 index for NGC 488, before and after correction, in Å. The white asterisks in the right-hand map mark the position of the centroids of the bins to which we have applied the correction. Overplotted on the maps are the isophotal contours. The two maps are plotted with the same cuts, indicated on their side, together with the colour bar; they are oriented with the horizontal and vertical axis aligned, respectively, to the long – and to the short – axis of the SAURON field.

### 3.1 Line strength measurement and Fe5015 correction

On the emission-removed spectra we calculated line strength indices on the Lick/IDS system. For details on the actual computation of the line strengths, we refer to Paper VI. The calibration to the Lick/IDS system takes into account several effects: the difference in spectral resolution between the Lick/IDS system and the SAURON instrumental set-up, the internal velocity broadening of the observed galaxies and small systematic offsets rising from differences in the shape of the continuum, due to the fact that the original Lick/IDS spectra have not been flux calibrated. In our observing run, we obtained spectra for 21 different stars in common with the Lick/IDS stellar library (Worthey et al. 1994), for a total of 39 repeated observations. Fig. 2 shows the difference between the Lick/IDS measurements and ours (for stars with repeated observations, we considered the average of the different values available). We calculated the mean offsets to the Lick/IDS system and their dispersion using bisquare weighting in order to minimize the influence of the outliers, after removing from the sample two stars of spectral type M6III and M7III, whose measured metal indices differ more than 2 Å from the Lick measurements. The adopted offsets that we applied to all our measurements are: −0.06 Å (± 0.06 Å) for H$\beta$, +0.32 Å (±0.15 Å) for Fe5015 and +0.15 Å (± 0.05 Å) for Mg$b$.

From a visual inspection of our maps of the Fe5015 index, we saw that our measurements tend to assume high values in the outer parts, especially in the bottom right-hand corner, revealing a systematic effect that makes the maps look asymmetric. The most striking manifestation of the problem is this 'high-iron corner', but there could be as well regions where the index is too low. A detailed inspection of the spectra showed that the cause is a wrong shape of the continuum in the Fe5015 spectral region, as proved by the fact that we are unable to fit our twilight spectra using our SSP template library: the Fe5015 region is not matched by the templates, and the Fe5015 map calculated on the twilight spectra is not flat over the field, showing a range of about 1.6 Å from minimum to maximum value. This continuum problem could be due to instrumental instabilities, to the high sensitivity of the grism to the incidence angle of the light, to the imperfect extraction of the spectra, to the misalignment of the spectra with respect to the columns of the CCD (see Ganda et al. 2006). We can exclude, instead, relations with problems in the gas removal, since the Fe5015 measurement is affected also in the twilight frame, where the spectra are gas-free. In addition to this, continuum problems should not influence the gas-cleaning procedure: in the fitting, a polynomial is included in order to account for differences in the flux calibration between the observed spectra and the model ones.

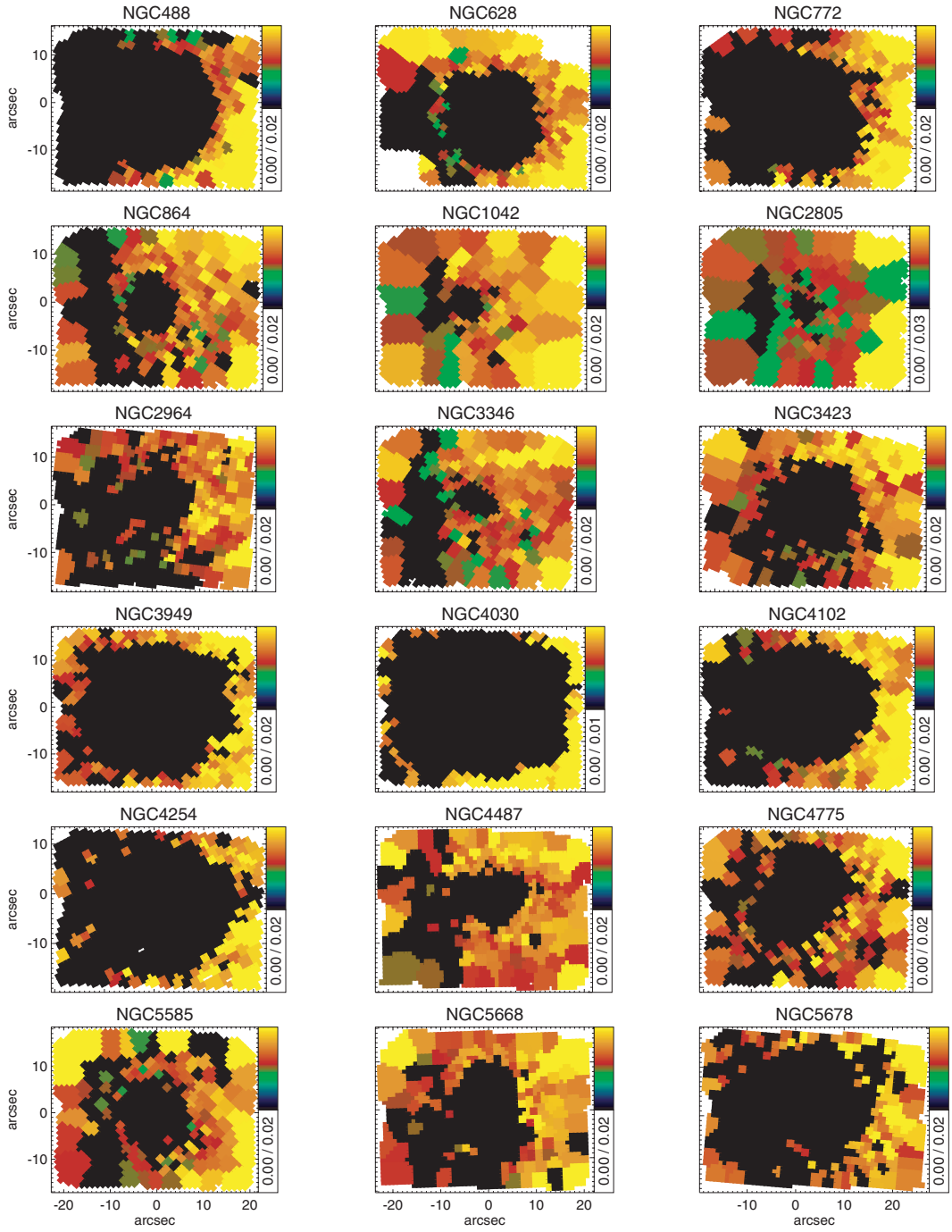


**Figure 5.** Galaxy-by-galaxy maps of the rms deviations of the fitted polynomial continuum after removal of a linear slope, in the correction procedure for the continuum problem affecting the Fe5015 measurement; in the bins in the black areas the correction will not be applied. All the maps are plotted with the same spatial scale and oriented with the horizontal and vertical axis aligned, respectively, to the long – and to the short – axis of the SAURON field.

Unfortunately, we could not take this effect into account properly at the data reduction stage, and decided to apply a correction to the affected spectra before measuring the Fe5015 index. A problem related to the shape of the continuum was experienced also for the early-type spirals of the SAURON survey and affected the H$\beta$ measurements, due to the closeness of the spectral feature to the edge of the spectral range; despite the fact that the problem is different, we worked out a correction similar to the one that was there applied in the case of H$\beta$ and described in Paper VI (section 3.1.2).

For each galaxy, we averaged the spectra within an aperture of 10 arcsec radius, obtaining a 'global spectrum' for that galaxy. We then fitted this global spectrum using a linear combination of SSP templates, masking the spectral regions possibly affected by emission lines. In this way we obtained for each galaxy a 'global optimal template' that approximates very well the general spectral features of that galaxy. Then we considered the two-dimensional galaxy's data cube, spatially binned and cleaned from emission as explained in the previous sections; for each bin, we fitted the cleaned

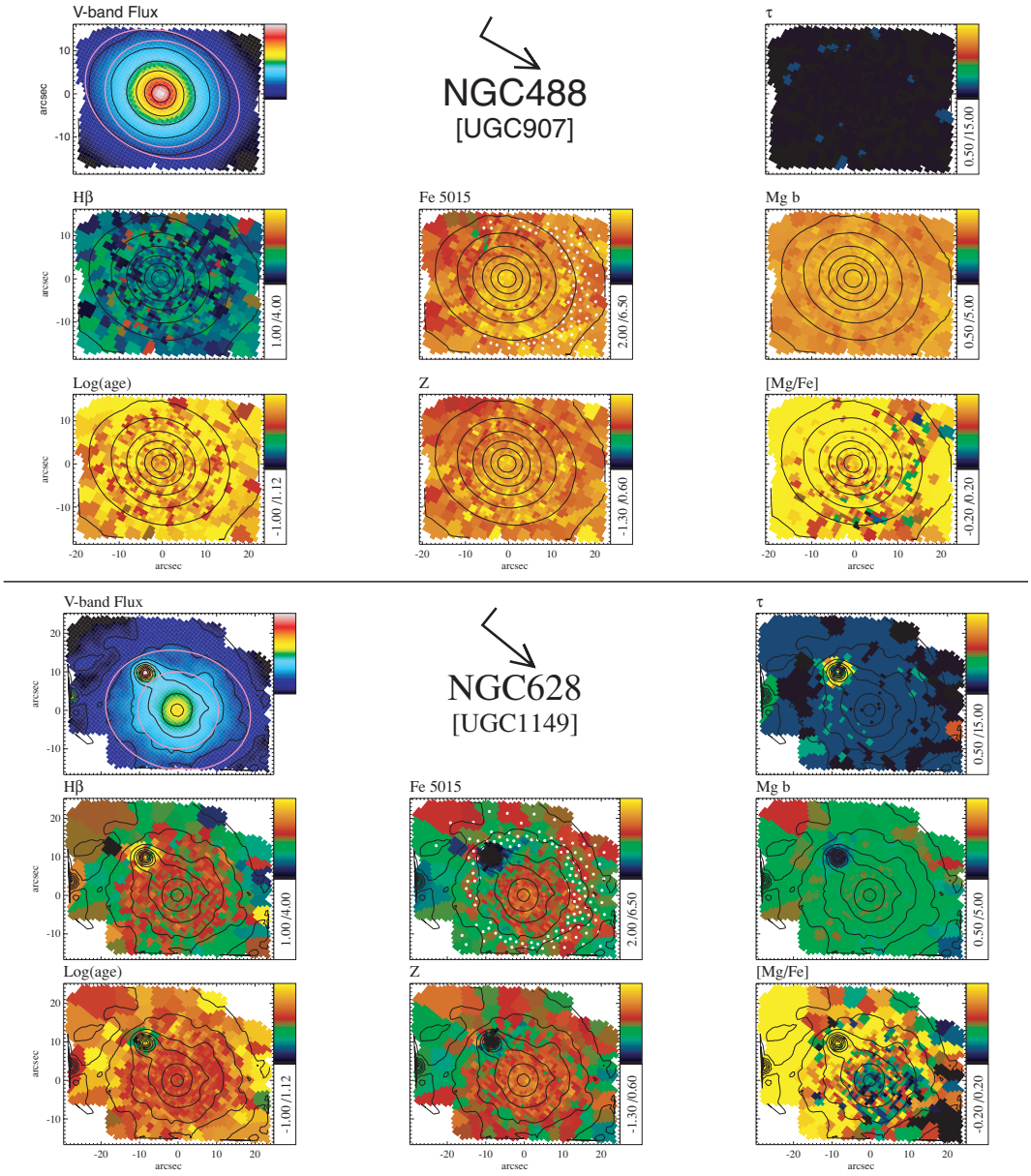


**Figure 6.** Maps for NGC 488 and 628. For each galaxy: first row: reconstructed image; NGC and UGC numbers and time-scale $\tau$ for star formation in Gyr; second row: maps of H$\beta$, Fe5015 and Mg*b* equivalent widths, in Å; the white dots on the Fe5015 map mark the bins where the correction described in Section 3.1 has been applied; third row: age (in units of decimal logarithm and measured in Gyr), metallicity and [Mg/Fe] abundance ratio from the one-SSP analysis. For a description of the methods, see Section 6. Overplotted on each map are the isophotal contours. On the intensity map also the contours defining the outer limits of the so-called 'bulge' and 'disc' regions (see Section 5) are overplotted, in pink. All the maps are presented with the same spatial scale; the arrow above the galaxy's name gives the direction of north and east. The plotting ranges are indicated together with the colour bar at the right-hand side of each map.

spectrum using the 'global optimal template' together with an 11th-order multiplicative polynomial, over the whole spectral range. The fit determined the best-fitting polynomial continuum, from which we then removed the linear component (which does not change the line indices); we considered the residuals and calculated their rms variation over the wavelength range of Fe5015. For bins covering four or more single-lens spectra and with an rms greater than 0.01, we used the fitted polynomial as a correction to the spectral shape by dividing it through the emission-cleaned spectrum. For these bins, we finally measured the Fe5015 index on the corrected spectrum.

This correction depends critically on the assumption that the optimal template is an accurate representation of the true galaxy spectrum. Whilst this is generally true, in the central, sometimes bulge-dominated, regions of our galaxies, non-solar abundance ratios can create a fit residual similar in size to the systematic effect we wish to remove. By correcting only bins containing four or more lenses, we avoid these central parts, since the data there are unbinned. Correcting large bins is also important because of their larger contribution to the spatial appearance of the maps.

We verified the Fe5015 correction using exposures of the twilight sky. As we mentioned above, in the twilight maps of Fe5015, a spatial gradient was also visible, as is apparent in the galaxy data. In the uncorrected twilight, the field centre gave values of Fe5015 close to ≈4 Å, consistent with a typical G2V–G4V sun-like

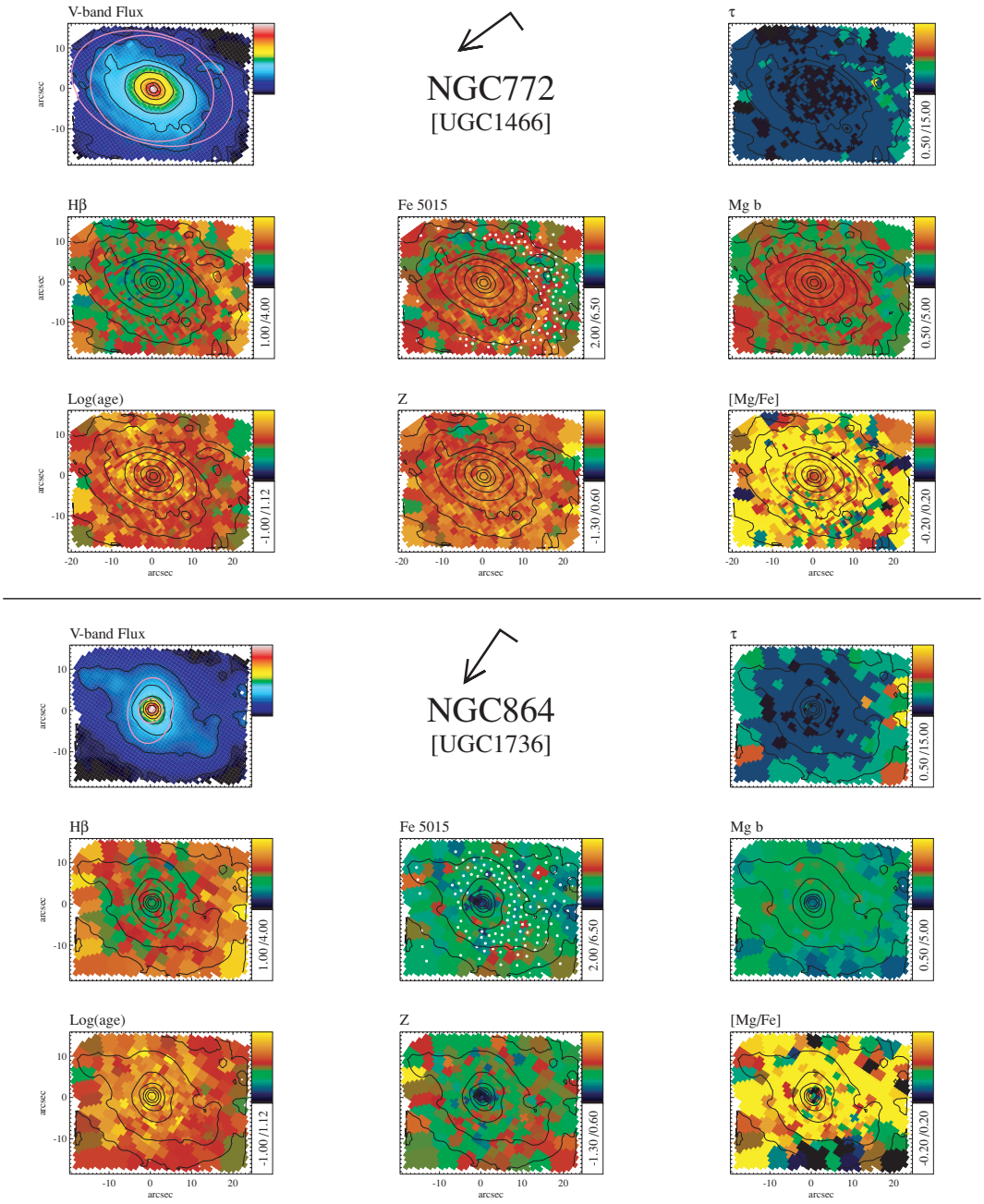


**Figure 7.** As in Fig. 6 but for NGC 772 and 864.

spectrum, showing that the field centre is not significantly affected by the problem. After applying our correction technique[2] the gradient was reduced, and the global level remained around 4 Å. We show this in Fig. 3, where we display the Fe5015 map calculated on the twilight frame, before and after applying the correction. Similarly, in Fig. 4 we show the Fe5015 map for NGC 488 before and after correction. White asterisks mark the centroids of the bins that have been corrected. The correction clearly removes most of the asymmetry, proving the usefulness of the method applied.

[2] Applied in this case to all single-lens spectra with an rms greater than 0.01: given the high S/N of the twilight frame, no spatial binning is necessary.

Fig. 5 presents for each galaxy the map of the rms deviations of the fitted continuum after removal of a linear slope. We plot in black the bins that do not meet the requirements for the correction, for which we have artificially put the rms to 0 (for plotting purposes only); in these bins the Fe5015 index is calculated on the original emission-cleaned spectra. The maps are oriented with the horizontal and vertical axis aligned, respectively, to the long – and to the short – axis of the SAURON field. The extension of the corrected area is mainly related to the S/N of the data: galaxies with poor S/N will require higher binning and the big bins will undergo the correction.

As for the uncertainties on the measured indices, the most worrying factor is the separation of emission and absorption lines. Simulations presented in appendix A of Paper V show that the

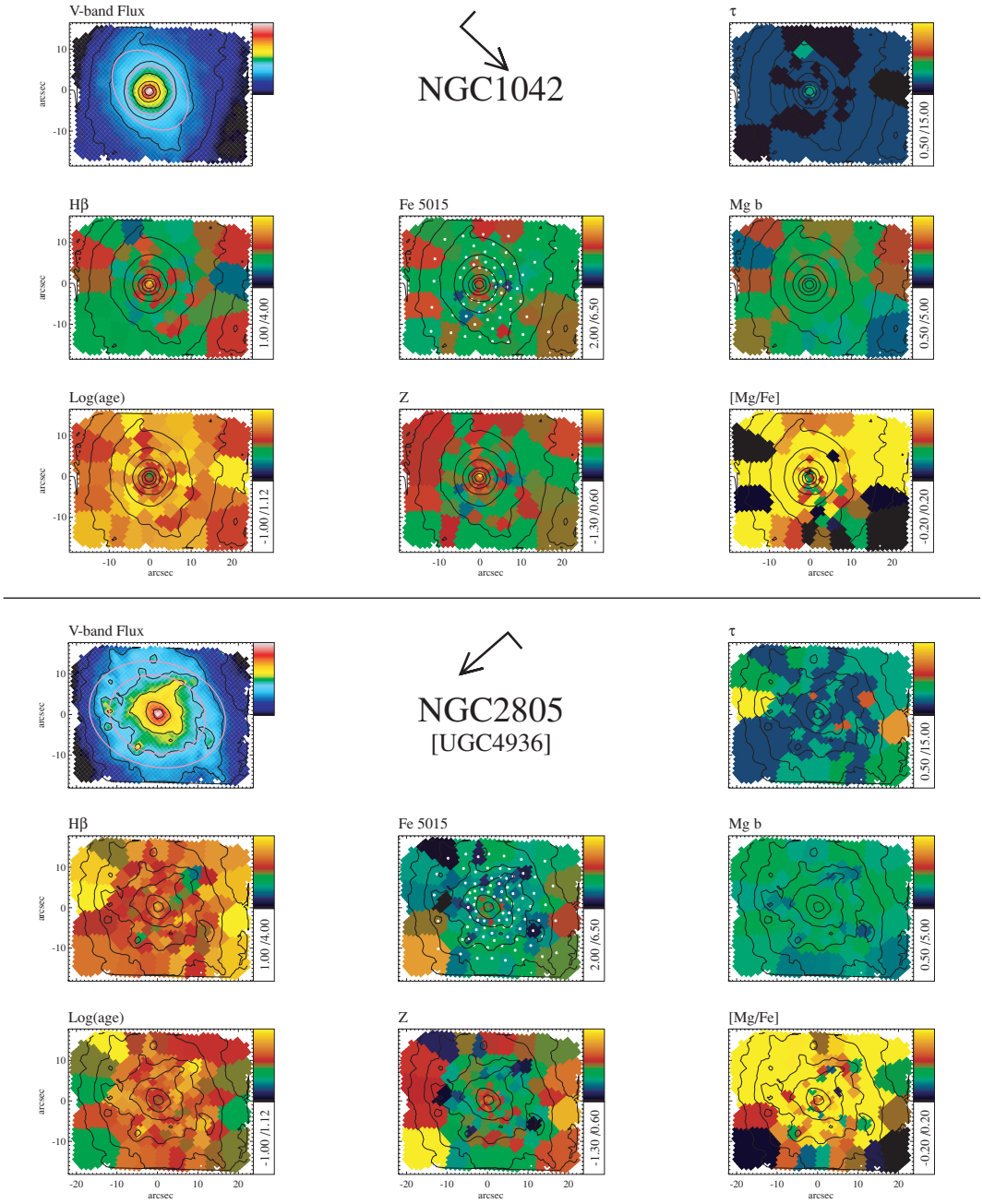


**Figure 8.** As in Fig. 6 but for NGC 1042 and 2805.

accuracy in recovering the emission line fluxes does not depend on the A/N ratio between the line amplitude and the noise level in the stellar continuum, but only on the S/N level in the stellar continuum itself. These simulations were meant to investigate the accuracy of emission line flux measurements for ellipticals and lenticulars. In the case of S/N = 60, the typical uncertainties in the line fluxes obtained in appendix A of Paper V translates in errors in the equivalent width of the emission line of ≈0.08 Å, and in similar errors in the absorption line indices. Paper XI presents absorption line strengths for early-type spirals observed with SAURON; in some of the galaxies studied there, the emission lines are stronger by a factor of up to 100, relative to the absorption lines, than in the ellipticals or lenticulars of Paper V with the strongest emission lines. Therefore, for the objects in Paper XI the situation is much closer to what happens in our spirals. There, the authors report results of similar simulations of the reliability of the gas cleaning, exploring a range in A/N ranging up to 100. The results are such that the errors in the absorption line indices do not vary appreciably with increasing A/N. When coming to the data, one has to consider that the spectra are packed close together, so that the absorption lines are affected by neighbouring spectra; despite the reduction tries to minimize this contamination, there might be some residual effects, particularly in presence of strong emission lines. Additional errors can derive from template mismatch in the fitting procedure and from the continuum correction described above. Therefore, throughout the rest of the paper we adopt a conservative value of 0.2 Å, for the uncertainties in H$\beta$ and Mg$b$ and 0.3 Å in Fe5015. The same figures were used in Paper XI.

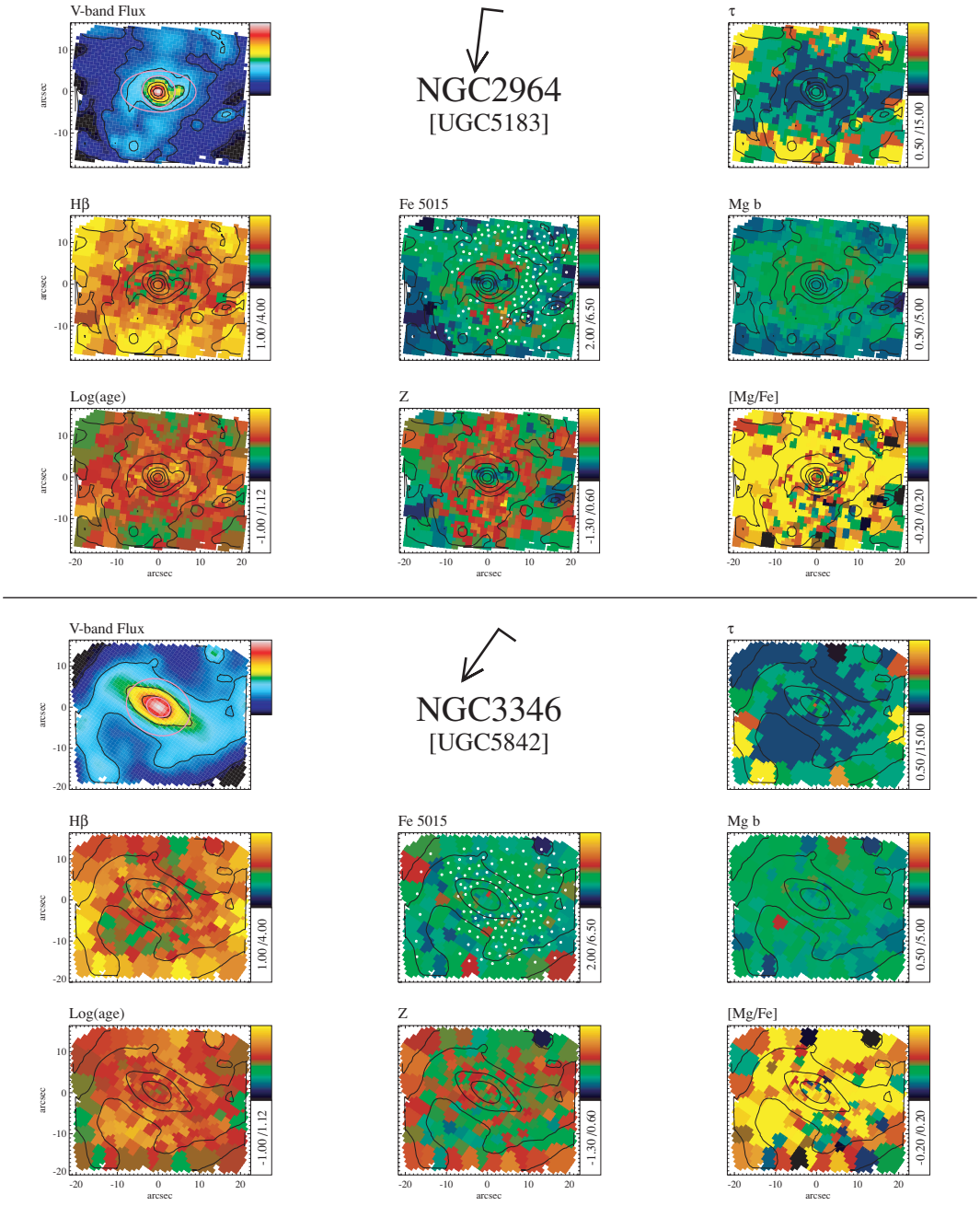


**Figure 9.** As in Fig. 6 but for NGC 2964 and 3346.

## 4 LINE STRENGTH MAPS OF 18 LATE-TYPE GALAXIES

Figs 6–14 present the absorption line strength maps of the 18 galaxies, ordered by increasing NGC number. For each galaxy, in the first row we show the total intensity obtained by integrating the full SAURON spectra in the wavelength direction, the galaxy NGC number (and the UGC also, when available), and the two-dimensional map of the characteristic time-scale of star formation $\tau$, in Gyr (see Section 6.3). Overlapped in pink on the intensity map are the contours delimiting the outer limits of the so-called 'bulge' and 'disc regions', defined in Section 5. In the second row we present the two-dimensional maps of H$\beta$, Fe5015 and Mg$b$, where the measured indices have been calibrated to the Lick/IDS system and are expressed in equivalent widths and measured in Å. The maps of Fe5015 have been corrected as explained in Section 3.1; the corrected bins are marked with a white dot. In the third row, we present the maps of age (expressed in units of decimal logarithm and measured in Gyr), metallicity (in units of decimal logarithm, with the solar metallicity as zero-point) and abundance ratios obtained with the one-SSP approach (see Section 6.1). Overplotted on each map are the isophotal contours. The maps are all plotted with the same spatial scale, and oriented with the horizontal and vertical axis aligned, respectively, to the long – and to the short – axis of the SAURON field for presentation purposes; the orientation is the same as in Ganda et al. (2006) and as in Figs 4 and 5 in this paper. The relative directions of north and east are indicated by the arrow above the galaxy's name. The maximum and minimum of the

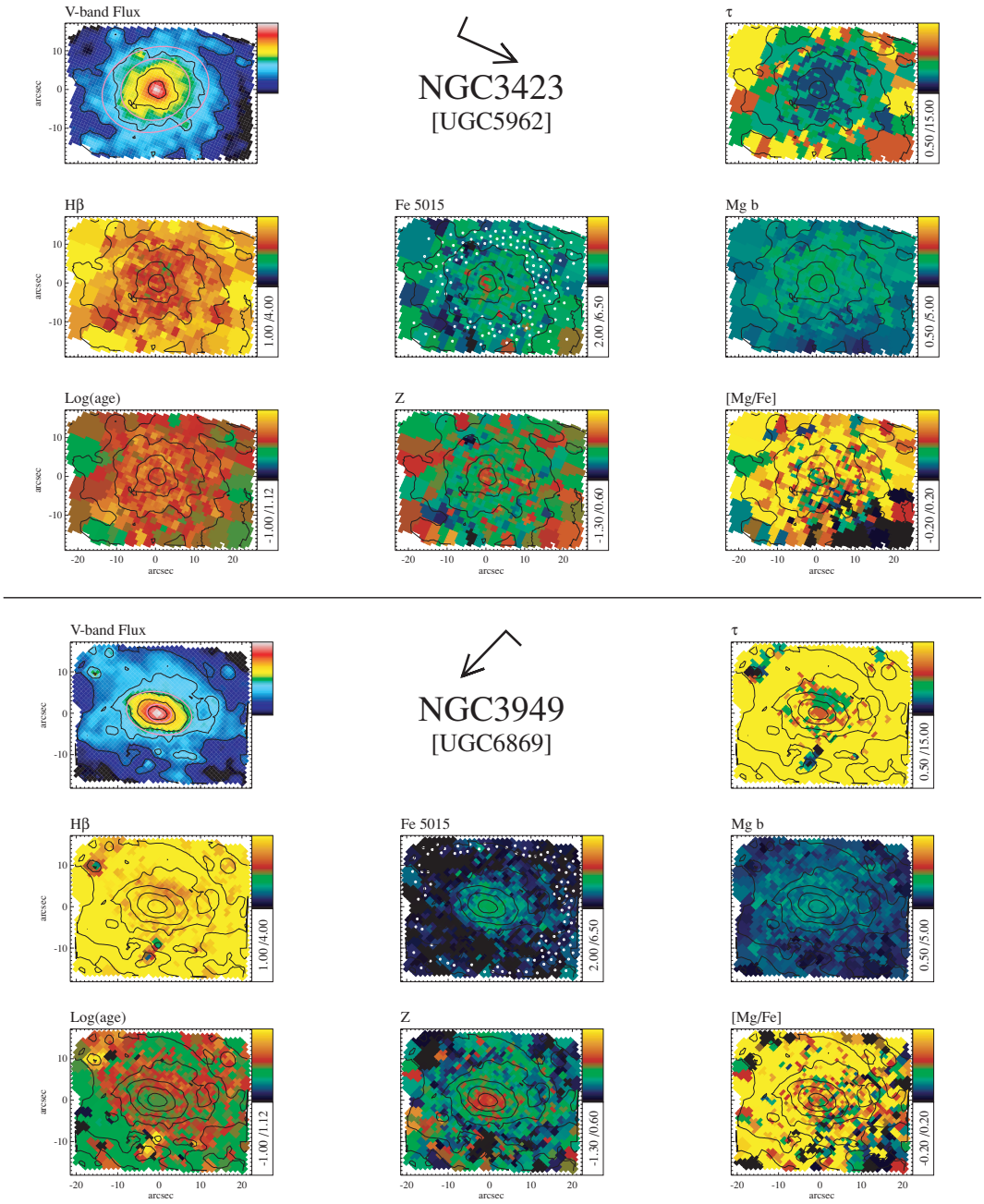


**Figure 10.** As in Fig. 6 but for NGC 3423 and 3949.

plotting ranges and the colour table are given in the tab attached to each map. To make the comparison among different objects more immediate, we adopted the same plotting ranges for all of the galaxies, but in Appendix B we will enlighten the spatial structures within the single maps, when noticeable, by inspecting the maps plotted on a 'galaxy-by-galaxy range'.

## 5 CORRELATIONS BETWEEN LINE STRENGTH INDICES AND OTHER GALACTIC PARAMETERS

In this Section we analyse the dependence between the line strength indices and other galactic parameters; we mainly focus on central properties. For each galaxy we defined three regions: the central circular aperture of 1.5 arcsec radius (corresponding to the innermost nine single-lens spectra); a so-called 'bulge region', defined as the region within which the light due to the fitted exponential disc falls below 50 per cent of the total light, with the exclusion of the central aperture; and a so-called 'disc region', a 3 arcsec thick elliptical annulus external to the 'bulge region'.[3] We averaged

[3] The inner semimajor axis of the 'disc region' corresponds to the outer semimajor axis of the 'bulge region' plus 2 arcsec. A slightly different definition of the disc region has been adopted in the case of NGC 628, in order to avoid contamination from a foreground star situated ≈13 arcsec south of the centre.

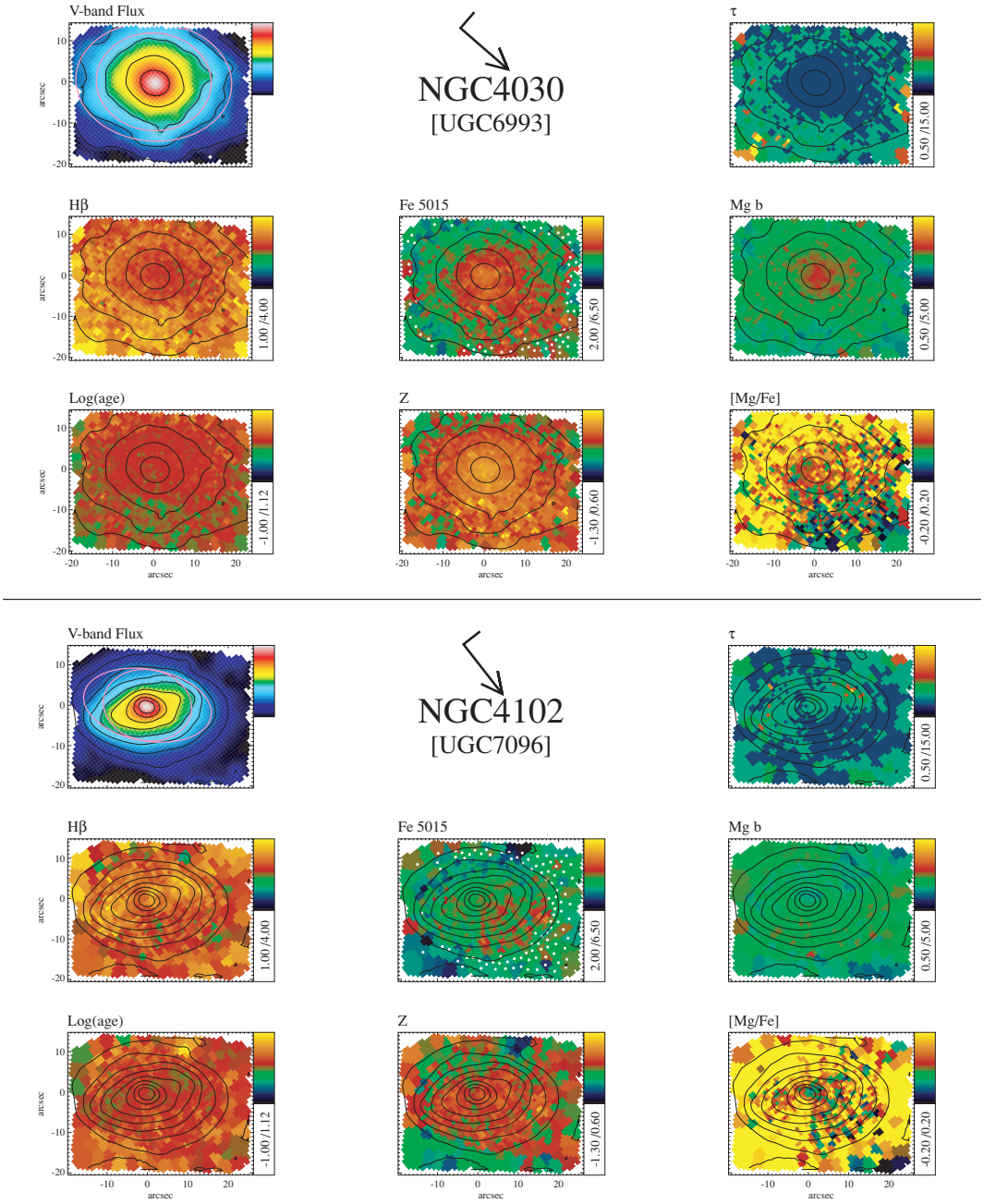


**Figure 11.** As in Fig. 6 but for NGC 4030 and 4102.

the spectra in these regions before spatial binning, and on the resulting spectrum calculated the line-strength indices, after emission removal.[4] The actual numbers for the definition of the bulge and disc regions (semimajor axis of the ellipses, position angles and ellipticities) were taken from our own photometric analysis and bulge–disc decomposition based on archival NIR images (Ganda et al., in preparation). There we model the galaxies as an exponential disc and a Sérsic (1968) bulge (which often turns out to be very tiny, with effective radius smaller than ≈5 arcsec) and apply a two-dimensional decomposition from which we can estimate the bulge extension (cf. Noordermeer & van der Hulst 2007 for the method and Ganda et al., in preparation, for the actual analysis of the profiles). For clarity, in the top left-hand map in Figs 6–14 we overplot in pink the elliptical contours defining the outer limits of the 'bulge region' and of the 'disc region'. In any case, we want to warn the reader that the 'bulge' and 'disc' regions here introduced are mainly a tool for us to investigate radial variations, and do not refer to distinct components, since the so-called 'bulge' is affected by a huge contamination from the disc, and an accurate decomposition is beyond the scopes of the present paper, and will be addressed in detail in the mentioned paper in preparation.

[4] For the aperture measurements, we never applied the continuum correction to the Fe5015 index described in Section 3.1: in several cases, even the disc region is affected only partially by the correction; in addition to this, the bulge and disc region measurements are obtained averaging spectra from spatially separated areas, which helps in minimizing the impact of the continuum problem in the Fe5015 spectral region.

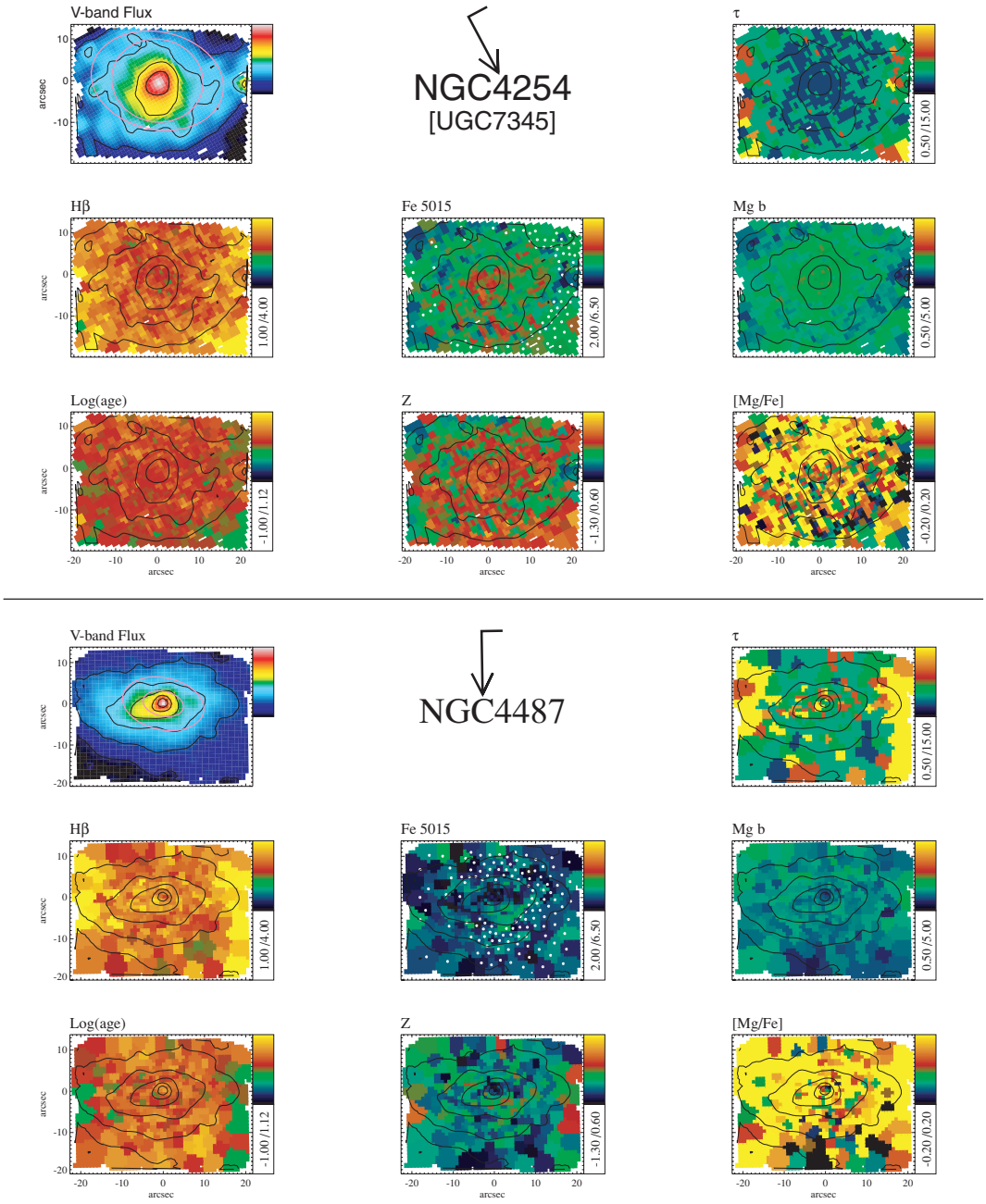


**Figure 12.** As in Fig. 6 but for NGC 4254 and 4487.

In Table 1 we list the morphological type (from the RC3) and the stellar velocity dispersion, with its associated error, measured on the central aperture spectra, since we will make use of these quantities in the following sections and figures; the errors on the velocity dispersion are based on the scatter of the velocity dispersion values that we measure for the single-lens spectra within the central aperture, and do not take into account template mismatch. Table 2 lists the index values calculated, galaxy by galaxy, on the central aperture and on the bulge and disc regions.

### 5.1 Index–index relations

In order to derive 'zero-order' estimates on the luminosity-weighted ages and metallicities of our galaxies, we show in Fig. 15 an age/metallicity diagnostic diagram. Here we use the abundance ratio insensitive index

$$[\mathrm{MgFe50}] = \frac{0.69 \times \mathrm{Mg}b + \mathrm{Fe5015}}{2} \quad (1)$$

(for details on the index definition see Kuntschner et al., in preparation) as metallicity indicator and H$\beta$ as age indicator. In Fig. 15, we plot the indices calculated on the central 1.5-arcsec aperture of our galaxies (black symbols). We overplot with red symbols the elliptical and lenticular galaxies from the SAURON survey (based on the data presented in Paper VI), with reference to measurements within apertures of radius 1.335 arcsec, that the authors of that paper extracted in order to match the Lick aperture (see Paper VI for details); the blue symbols represent central apertures of 1.2 arcsec radius for

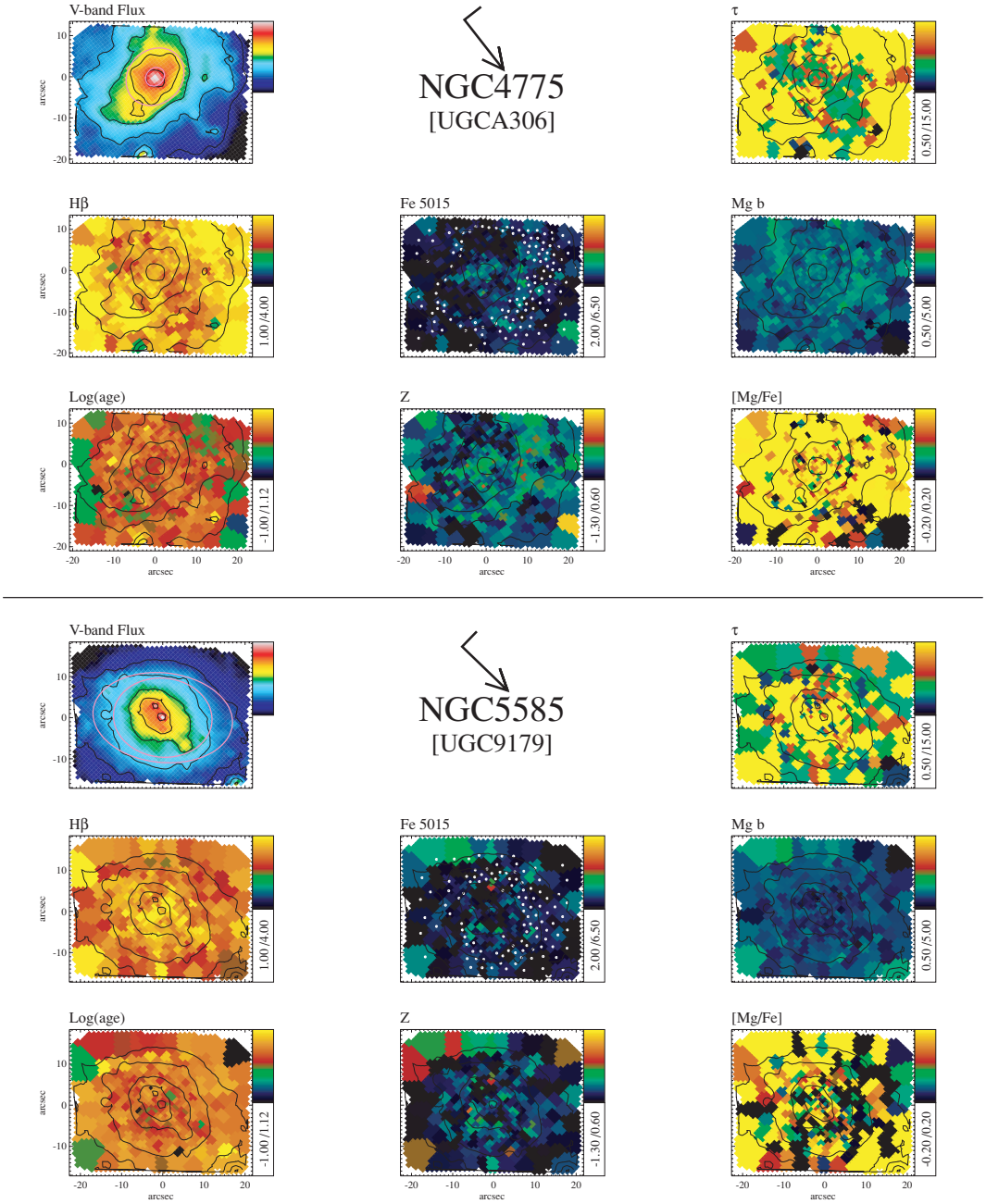


**Figure 13.** As in Fig. 6 but for NGC 4775 and 5585.

the early-type spirals from the same survey (Paper XI). Overplotted in the figure are also the models of Thomas, Maraston & Bender (2003), limited to the models with [Mg/Fe] = 0; they are labelled with the corresponding age and metallicity. As noted in Paper XI, there is a smooth transition between the ellipticals/lenticulars and the early-type spirals, with most E/S0 populating the region of the old, metal-rich models, and the Sa spanning a larger range in age and reaching lower metallicities. Our 18 later type spirals occupy a region of the diagram that has little intersection with the E/S0s, having generally younger ages and being clearly more metal-poor. We also note that the parameter region occupied by our galaxies is completely included in the one spanned by the Sa galaxies. We warn the reader that the interpretation in terms of ages and metallicities is here done on the basis of SSP models, which might not provide a good description of spiral galaxies, for which the star formation history could be characterized by several bursts spread over time or by a constant SFR. A more detailed analysis of the age, metallicities and the star formation history is presented in Section 6.

In Fig. 16 the left-hand panel shows the line index Fe5015 against Mg*b* for the central aperture of our 18 galaxies (black symbols); as in Fig. 15, we show also the points corresponding to the E/S0 (red symbols) and Sa (blue) of the SAURON survey. The solid lines represent the SSP model grid from Thomas et al. (2003) with [Mg/Fe] = 0; the dashed lines correspond instead to the Thomas models with [Mg/Fe] = 0.5. As also shown in Paper XI with a similar figure, it is clear that most of the ellipticals can be fitted better by models overenhanced in $\alpha$-elements, while the Sa bulges present a range in enhancement. Our later type spirals instead are

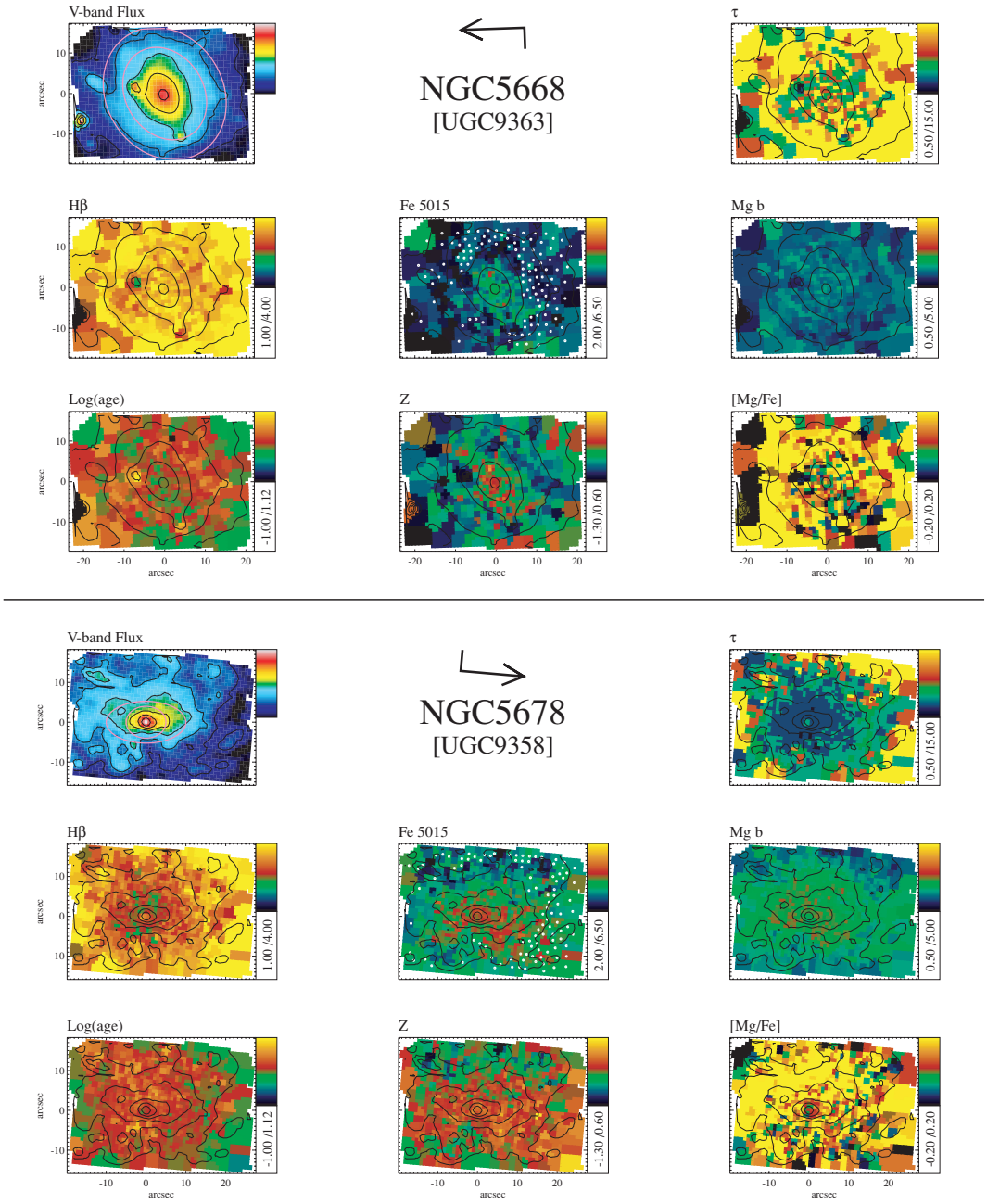


**Figure 14.** As in Fig. 6 but for NGC 5668 and 5678.

in all cases compatible with models with solar abundance ratios. In the middle and left-hand panels we show, only for our sample of late-type spirals, the measurements for the previously defined bulge and disc regions, respectively, in the (Mg*b*, Fe5015) plane, along with the models from Thomas et al. (2003), drawn only in the case of solar abundance ratios. We see that our spirals are compatible with solar abundance ratios, within the uncertainties; we do not detect relevant global variations in the appearance of the diagram when considering the different regions (central aperture, bulge and disc region): the single galaxies move in the diagram, but they remain in the region of the models with solar abundance ratios. This differs from what seen in the early-type spirals of the SAURON survey: there, away from the centre (≈10 arcsec from the centre) the galaxies have generally higher [Mg/Fe] than in the centre. Supersolar abundance ratios are possibly caused by the presence of populations with several ages. An increase of [Mg/Fe] when moving outwards is detected also by Jablonka (2007) and Moorthy & Holtzman (2006) for samples of galaxies of type varying between S0 and Sc. This might be due to a change from SSP-like stellar populations in the centre to populations with a large range in age outside. In particular, Jablonka (2007) measures small increments in abundance ratio from the central region to the bulge effective radius; these gradients stay rather constant among bulges; Moorthy & Holtzman (2006) find that most of their galaxies have positive or zero gradient in [Mg/Fe] within the bulge-dominated region; as mentioned in Section 1, they divide their sample in red ($B - K > 4$) and blue bulges, and, according to their analysis, the red bulges are overabundant in the centre, while the blue bulges have solar abundance ratios in

**Table 1.** Hubble type (RC3 through NED); numerical morphological type (from RC3, indicated as 'T-type' in some of the following pictures); stellar velocity dispersion (in km $s^{-1}$) and its associated error, also in km $s^{-1}$, measured on the central aperture spectrum, for all galaxies.

| NGC | Type | $T$ | $\sigma$ | $\pm\Delta\sigma$ |
|---|---|---|---|---|
| 488 | SA(r)b | 3.0 | 197 | 4 |
| 628 | SA(s)c | 5.0 | 52 | 6 |
| 772 | SA(s)b | 3.0 | 120 | 4 |
| 864 | SAB(rs)c | 5.0 | 65 | 20 |
| 1042 | SAB(rs)cd | 6.0 | 55 | 13 |
| 2805 | SAB(rs)d | 7.0 | 46 | 18 |
| 2964 | SAB(r)bc | 4.0 | 102 | 11 |
| 3346 | SB(rs)cd | 6.0 | 48 | 23 |
| 3423 | SA(s)cd | 6.0 | 48 | 20 |
| 3949 | SA(s)bc | 4.0 | 60 | 10 |
| 4030 | SA(s)bc | 4.0 | 100 | 2 |
| 4102 | SAB(s)b? | 3.0 | 153 | 8 |
| 4254 | SA(s)c | 5.0 | 72 | 13 |
| 4487 | SAB(rs)cd | 6.0 | 51 | 21 |
| 4775 | SA(s)d | 7.0 | 41 | 21 |
| 5585 | SAB(s)d | 7.0 | 37 | 23 |
| 5668 | SA(s)d | 7.0 | 52 | 22 |
| 5678 | SAB(rs)b | 3.0 | 102 | 9 |

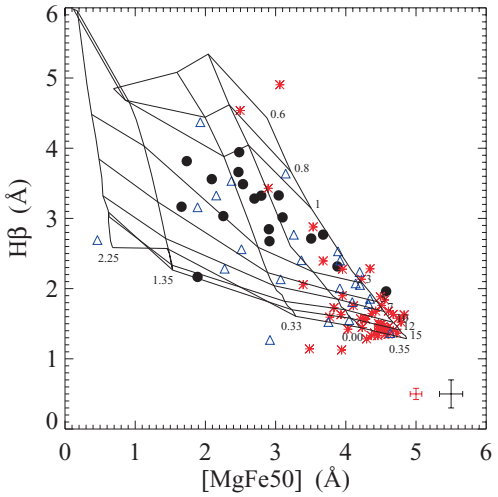


**Figure 15.** H$\beta$ index against [MgFe50] (in Å), for three samples of galaxies observed with SAURON: the black symbols represent the central apertures of our late-type spirals, the red symbols are the E and S0 (central aperture of 1.335 arcsec radius) and the blue ones the Sa galaxies (central aperture). The solid lines represent SSP models from Thomas et al. (2003), limited to models with solar abundance ratios; ages of the models vary from 0.6 to 15 Gyr (top to bottom); metallicity (in decimal logarithm) from −2.25 to +0.35 (left- to right-hand side). Representative error bars are added at the bottom right-hand side of the panel; the black one refers to both the early- and late-type spiral samples, while the red one, smaller, refers to the E/S0 galaxies.

the centre, and the disc-dominated regions also have approximately solar abundance ratios. Therefore, our results are not necessarily in contradiction with theirs, as we will also see in Appendix A, where we briefly discuss the radial profiles of the indices and the population parameters.

### 5.2 Index–Hubble type relations

The three panels in Fig. 17 present the relation between the central line indices (respectively, H$\beta$, Fe5015 and Mg*b*) and the morphological type (see Table 1). Again, we use black symbols for the 18 late-type spirals under investigation, red ones for the ellipticals and lenticulars and blue for the early-type spirals of the SAURON survey. We see an overall increase of H$\beta$ and a decrease of Fe5015 and Mg*b* going towards later types. We also see that for ellipticals the range spanned in equivalent width is in general quite small, it becomes larger for lenticulars and Sa galaxies and smaller again in the later type spirals. This result is illustrated quantitatively in Table 3, where we list for each index the range in equivalent width spanned in the three samples, together with the minimum and maximum values assumed by the indices: as one can see, the range in H$\beta$ is larger for the E/S0 than for the Sa sample, while for the other indices the range is larger for the early-type spirals; in all three indices, the Sb–Sd galaxies span a narrower range than the Sa. In

**Table 2.** Line strength indices calculated on the central apertures and bulge and disc regions, defined as explained in Section 5 for the 18 galaxies. The indices are intended as equivalent widths and expressed in Å.

| NGC | H$\beta_{\rm centre}$ | H$\beta_{\rm bulge}$ | H$\beta_{\rm disc}$ | Fe5015$_{\rm centre}$ | Fe5015$_{\rm bulge}$ | Fe5015$_{\rm disc}$ | Mg$b_{\rm centre}$ | Mg$b_{\rm bulge}$ | Mg$b_{\rm disc}$ |
|---|---|---|---|---|---|---|---|---|---|
| 488 | 1.961 | 1.966 | 1.961 | 6.122 | 5.635 | 5.615 | 4.387 | 4.112 | 4.042 |
| 628 | 2.713 | 2.604 | 2.486 | 5.247 | 4.556 | 3.936 | 2.561 | 2.424 | 2.274 |
| 772 | 2.316 | 2.355 | 2.765 | 5.495 | 4.746 | 4.506 | 3.285 | 3.028 | 2.558 |
| 864 | 2.167 | 2.380 | 2.404 | 2.697 | 3.115 | 3.686 | 1.564 | 1.859 | 2.378 |
| 1042 | 3.327 | 2.533 | 2.172 | 4.570 | 4.046 | 3.767 | 2.200 | 2.498 | 2.356 |
| 2805 | 3.324 | 2.878 | 3.013 | 3.975 | 3.400 | 3.303 | 2.343 | 2.121 | 2.058 |
| 2964 | 3.033 | 2.957 | 2.808 | 3.313 | 3.476 | 4.025 | 1.736 | 2.049 | 2.264 |
| 3346 | 3.488 | 3.289 | 2.838 | 3.732 | 3.643 | 3.915 | 1.939 | 2.002 | 2.247 |
| 3423 | 2.846 | 2.935 | 3.299 | 4.334 | 3.528 | 3.092 | 2.137 | 1.869 | 1.692 |
| 3949 | 3.944 | 3.846 | 3.726 | 3.760 | 3.623 | 3.175 | 1.744 | 1.772 | 1.505 |
| 4030 | 2.769 | 3.086 | 3.343 | 5.287 | 4.512 | 3.886 | 2.996 | 2.524 | 2.144 |
| 4102 | 3.283 | 3.257 | 3.173 | 4.083 | 3.950 | 3.736 | 1.904 | 2.143 | 2.121 |
| 4254 | 2.676 | 2.955 | 3.177 | 4.121 | 3.954 | 3.699 | 2.470 | 2.149 | 1.864 |
| 4487 | 3.167 | 3.452 | 3.275 | 2.410 | 2.692 | 3.175 | 1.319 | 1.487 | 1.666 |
| 4775 | 3.560 | 3.482 | 3.465 | 3.071 | 2.980 | 2.376 | 1.609 | 1.564 | 1.412 |
| 5585 | 3.816 | 3.490 | 3.236 | 2.643 | 2.453 | 2.354 | 1.198 | 1.201 | 1.351 |
| 5668 | 3.661 | 3.584 | 3.825 | 3.756 | 3.037 | 2.546 | 1.717 | 1.464 | 1.265 |
| 5678 | 3.015 | 2.617 | 2.881 | 4.566 | 4.328 | 4.112 | 2.367 | 2.484 | 2.380 |

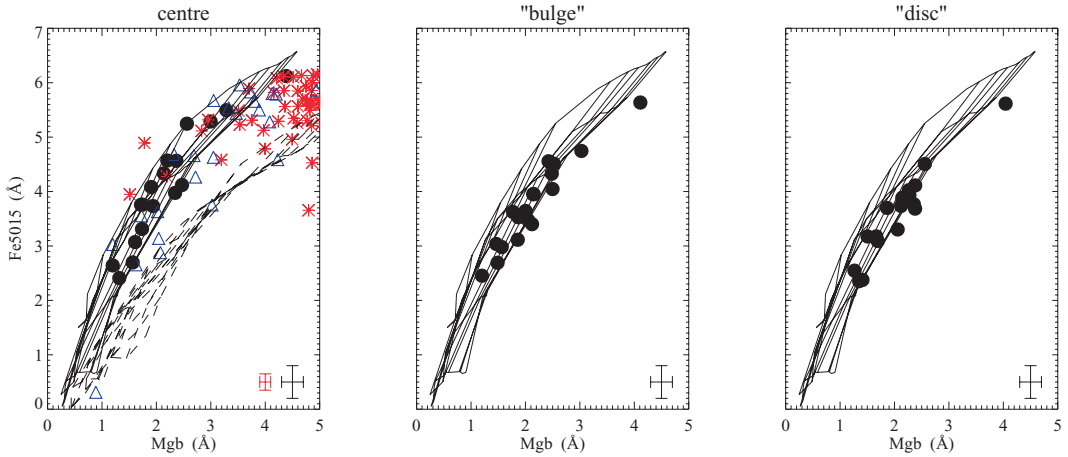


**Figure 16.** Left-hand panel: index–index diagram showing Fe5015 against Mg*b* for the central aperture of our late-type spirals (black symbols), while the red symbols are the E and S0 (within a 1.335 arcsec central aperture) and the blue ones the Sa (central aperture), observed with SAURON. The solid lines represent the SSP models from Thomas et al. (2003), limited to models with solar abundance ratios; the dashed lines correspond instead to the models with [Mg/Fe] = 0.5. Middle panel: same as the previous, for the 'bulge region' apertures of the 18 late-type spirals only. Right-hand panel: same as the previous, for the 'disc region' apertures of the 18 late-type spirals only; in the middle and right-hand panels we only plot the model grid for solar abundance ratios. All the indices are expressed as equivalent width and measured in Å; the three panels share the same vertical axis. Representative error bars are added at the bottom right-hand side of each panel; the black one refers to both the early- and late-type spiral samples, while the red one refers to the E/S0 galaxies.

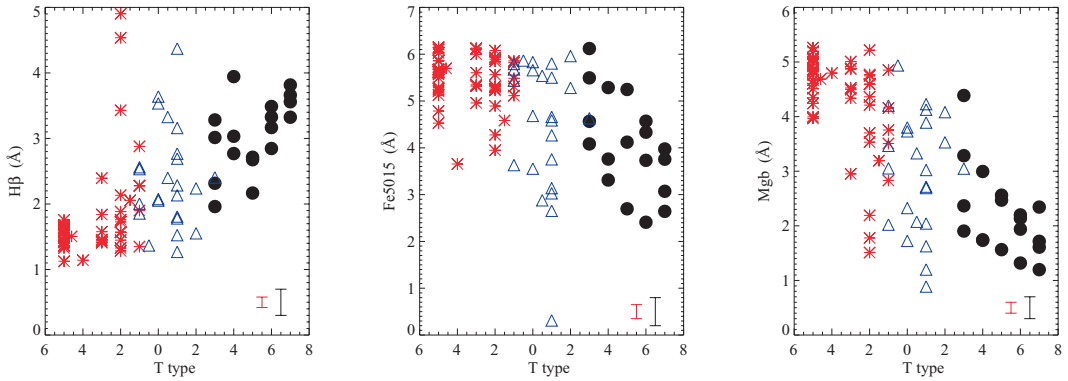


**Figure 17.** Line strength indices (in Å) as function of morphological type. Black symbols are our sample galaxies (central aperture), red are the E and S0 (central 1.335-arcsec aperture) and blue the Sa galaxies (central aperture) of the SAURON survey. The left-hand panel refers to H$\beta$, the middle one to Fe5015 and the right-hand panel to Mg*b*. Representative error bars are added at the bottom right-hand side of each panel; the black one refers to both the early- and late-type spiral samples, while the red one refers to the E/S0 galaxies.

the same table, we also list the average value of the indices in the three samples, together with their standard deviation and the standard deviation after subtraction of the observational errors, which indicates the amount of scatter that cannot be explained by the errors.

### 5.3 Index–velocity dispersion relation

Fig. 18 shows the central Mg*b* and H$\beta$ indices against the central velocity dispersion of the stars (see Table 1), in the left- and right-hand panels, respectively. As in the previous figures, the black symbols represent the late-type galaxies, the red the ellipticals and lenticulars and the blue the Sa observed with SAURON (central apertures). In these plots we express the indices in magnitudes, as it is often done in the literature, using the definition

$$\mathrm{index}' = -2.5 \log \left(1 - \frac{\mathrm{index}}{\Delta\lambda}\right), \quad (2)$$

where index and index$'$ are measured, respectively, in Å and magnitudes and $\Delta\lambda$ is the width of the index bandpass (cf. Paper VI for the full index definition).

A tight and well-known relation between magnesium indices (Mg$b'$ or $\mathrm{Mg}_2$) and $\sigma$ holds for ellipticals (see e.g. Terlevich et al. 1981; Burstein et al. 1988; Bender, Burstein & Faber 1993; Jørgensen et al. 1996; Colless et al. 1999; Falcón-Barroso et al. 2002; Bernardi et al. 2003; Worthey & Collobert 2003; Denicoló et al. 2005). In Fig. 18 (left-hand panel), we overplot with a black solid line the relation obtained by Jørgensen et al. (1996) for a sample of 207 E and S0 galaxies in 10 clusters:

$$\mathrm{Mg}_2 = 0.196 \log(\sigma) - 0.155, \quad (3)$$

after having converted the $\mathrm{Mg}_2$ index to Mg$b'$ using a least-squares fit to all the models from Vazdekis et al. (1996) with $\mathrm{Mg}_2 > 0.10$, holding the relation

$$\mathrm{Mg}b' = 0.489 \times \mathrm{Mg}_2 + 0.014. \quad (4)$$

**Table 3.** Upper part: ranges spanned in equivalent width (Å) by the three indices, for the three samples represented in Fig. 17; between brackets are indicated the minimum and maximum values. Lower part: average values of the indices in the three samples, with the relative standard deviations; the numbers in parenthesis indicate the standard deviation after subtraction of the observational error.

| Index | E/S0 | Sa | Sb–Sd |
|---|---|---|---|
| $H\beta_{range}$ | 3.78 [1.13–4.90] | 3.10 [1.27–4.37] | 1.98 [1.96–3.94] |
| $Fe5015_{range}$ | 2.50 [3.66–6.15] | 5.65 [0.31–5.96] | 3.71 [2.41–6.12] |
| $Mgb_{range}$ | 3.75 [1.51–5.26] | 4.05 [0.89–4.94] | 3.19 [1.20–4.39] |
| $\langle H\beta\rangle \pm \sigma$ | $1.79 \pm 0.75$ (0.67) | $2.39 \pm 0.77$ (0.57) | $3.06 \pm 0.56$ (0.36) |
| $\langle Fe5015\rangle \pm \sigma$ | $5.45 \pm 0.56$ (0.41) | $4.51 \pm 1.40$ (1.10) | $4.06 \pm 1.04$ (0.74) |
| $\langle Mgb\rangle \pm \sigma$ | $4.33 \pm 0.87$ (0.77) | $2.99 \pm 1.07$ (0.87) | $2.19 \pm 0.77$ (0.57) |

**Table 4.** Coefficients of the index$' - \sigma$ relation, in the form: index$' = a_{\rm index'} + b_{\rm index'} \times \log(\sigma)$; the first column lists the references (Jor = Jørgensen et al. (1996); $San_{LD}$ = Sánchez-Blázquez et al. (2006), low-density environment; $San_{HD}$ = Sánchez-Blázquez et al. (2006), high-density environment; KG = this work), the second and third columns list the coefficients for the relation with Mg$b'$, the fourth and fifth columns list the coefficients for the relation with H$\beta'$.

| Reference | $a_{Mgb'}$ | $b_{Mgb'}$ | $a_{H\beta'}$ | $b_{H\beta'}$ |
|---|---|---|---|---|
| Jor | −0.062 | 0.096 | – | – |
| $San_{LD}$ | −0.073 | 0.1 | 0.130 | −0.030 |
| $San_{HD}$ | −0.050 | 0.091 | 0.087 | −0.012 |
| KG | −0.093 | 0.092 | 0.247 | −0.068 |

One could think that this transformation, using models that do not take into account differences in abundance ratios, could be misleading. But in practice the Mg$b'$−$Mg_2$ relation has very little scatter, even for different [Mg/Fe]. In any case, we also compare the position of our spirals in the ($\log(\sigma)$, Mg$b'$) plane with the relations determined by Sánchez-Blázquez et al. (2006) in a fully empirical way for a sample of 98 early-type galaxies drawn from different environments (the field, poor groups, Virgo, Coma and some Abell clusters). The black dotted and dash–dotted lines overplotted in Fig. 18 represent their fitted Mg$b'$−$\sigma$ relation for low- and high-density environments, respectively, and lie both very close to the relation of Jørgensen et al. (1996), especially for high velocity dispersions; similarly, in the right-hand panel we overplot their H$\beta$−$\sigma$ relations. The relations of Jørgensen et al. (1996) and Sánchez-Blázquez et al. (2006) are both determined performing a fit down to velocity dispersions below 100 km s$^{-1}$ (≈40 km s$^{-1}$ in the case of Sánchez-Blázquez et al. 2006), therefore exploring the range of velocity dispersions that we test with our late-type spirals. The small differences between these relations might be due to the different statistics and to the different environments: Jørgensen et al. (1996) themselves noted that the relation differs slightly from cluster to cluster, in the sense that galaxies in clusters with lower $\sigma$ have systematically lower $Mg_2$. We also performed a linear fit to our own data: the green solid line overplotted in both panels represents the corresponding relation.

In Table 4 we list the coefficients defining the relations taken from the literature, together with the coefficients determined for our own sample, in the form

$$\text{index}' = a'_{\rm index} + b'_{\rm index} \log(\sigma). \quad (5)$$

As already pointed out in Paper XI for the Sa galaxies of the SAURON survey (blue symbols in the figure), it is clear from Fig. 18 and from Table 4 that the Mg$b'$−$\sigma$ relation for ellipticals represents an upper envelope for the spirals; some of the spirals follow the relation (particularly if we consider the Sa), but the majority of them lie below it; in particular, the linear fit to our own data (green line) runs almost parallel to the line from Jørgensen et al. (1996), but significantly below it. Similarly, in the case of the H$\beta'$−$\sigma$ relation, the ellipticals represent a lower envelope (see Paper XI) and many spirals lie above the relation. Deviations from the relations for early-type galaxies may be driven by stochastic processes like star formation: as argued by Schweizer & Seitzer (1992), the line defined by the galaxies of Jørgensen et al. (1996) corresponds to old stellar populations, while the deviations would be due to younger

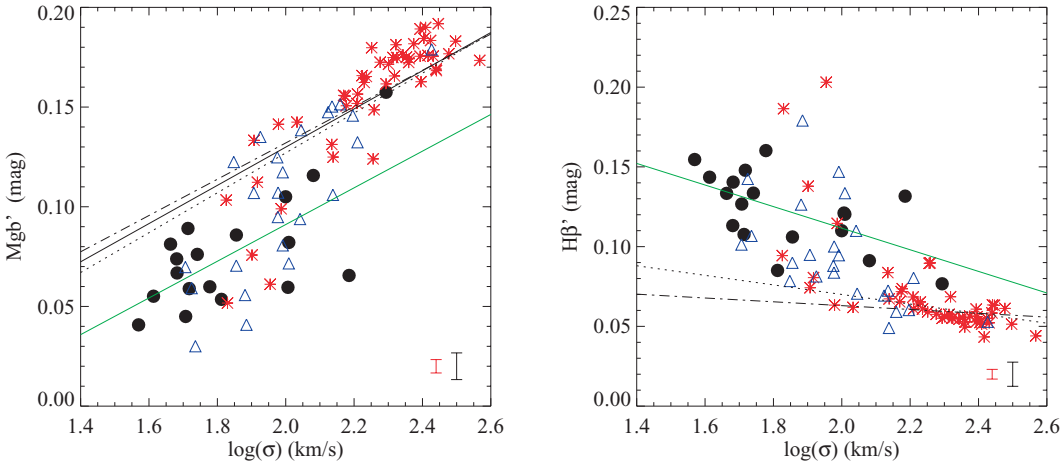


**Figure 18.** Left-hand panel: central Mg$b'$, expressed in magnitudes, against central velocity dispersion, in units of decimal logarithm. The black symbols represent our own sample (central aperture), the red the E and S0 and the blue the Sa galaxies of the SAURON survey. Right-hand panel: central H$\beta'$, expressed in magnitudes, against central velocity dispersion, in units of decimal logarithm; the colour code for the symbols is the same as in the previous case. The black solid line overplotted in the left-hand panel represents the relation found by Jørgensen et al. (1996) for early-type galaxies in 10 cluster. The dotted and dash–dotted black lines overplotted in both panels are the relations obtained by Sánchez-Blázquez et al. (2006) for low- and high-density environments, respectively, and the green solid lines are the relations determined using our own sample; see text in Section 5.3 for details. Representative error bars are added at the bottom right-hand side of each panel; the black one refers to both the early- and late-type spiral samples, while the red one refers to the E/S0 galaxies.

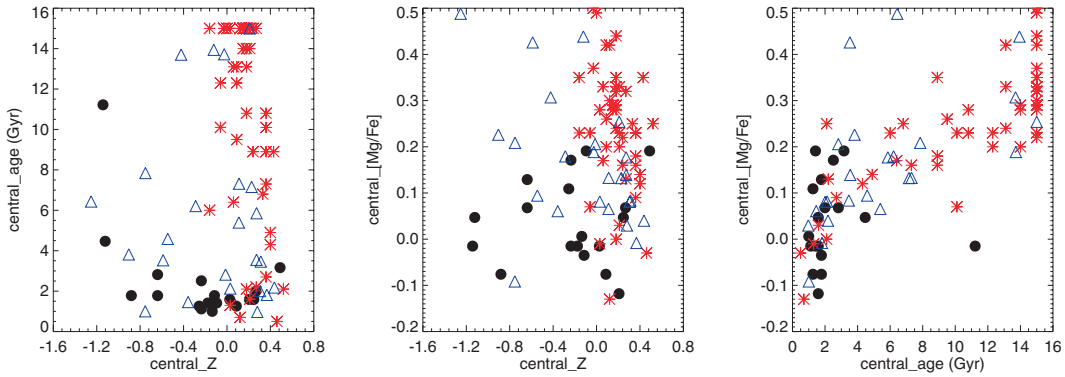


**Figure 19.** Central aperture values of the stellar population parameters from our one-SSP analysis. Left-hand panel: central age (in Gyr) against central metallicity (in decimal logarithm, with the solar metallicity as zero-point); middle panel: central abundance ratio against central metallicity; right-hand panel: central abundance ratio against central age. In black we represent our sample galaxies, while in red the E and S0 and in blue the Sa galaxies observed with SAURON.

stars. For our objects (black dots) the effect of young populations as deviation from the line defined by E/S0s galaxies is evident.

## 6 AGE, METALLICITY, STAR FORMATION HISTORY

The ultimate aim of measuring line strengths is to understand the distribution of stellar ages, metallicities and abundance ratios, and to get hints on the star formation histories. Using a combination of line-strength indices, one can constrain stellar population models, which allow us to translate the line-strength values into measurements of age, metallicity and abundance ratio.

Trying to address this issue, we investigated two main approaches: from one side, one can assume that a galaxy can be viewed as an SSP, and compare observations with theoretical SSPs in order to determine the best-fitting population; this is a 'classical' approach to stellar population studies. From the other side, one can view a galaxy's population as the time evolution of an initial SSP; making some assumptions on the initial metallicity and the metal enrichment history, by comparison of observations and models one can retrieve information on the star formation history. Nowadays, this is a topic of greatest interest: recently, several groups have been working on it and developed tools. Here we mention noticeable examples such as STECMAP and its extension STECKMAP[5] and MOPED. STECMAP and STECKMAP have been developed by Ocvirk and collaborators (for a description, see Ocvirk et al. 2006a,b), and try to recover the star formation history via spectral fitting, without any a priori assumption on the star formation history; the only condition imposed is that the star formation history is a smooth function of time; MOPED, developed by Panter and collaborators, is a method that allows to analyse huge quantities of spectra using the entire spectral range, and assumes that a galaxy can be viewed as superposition of single bursts (for details see Panter, Heavens & Jimenez 2003).

In this section we will follow these two roads (SSP and recovery of star formation history), on the basis of our measured Lick indices.

### 6.1 Single stellar population analysis

Following the examples of Paper VIII and Paper XI, we used the single-burst stellar population models of Thomas et al. (2003) to compare with our observations and estimate the ages, metallicities and abundance ratios of our galaxies. To avoid strong discretization effects on the derived parameters, we interpolated the original grid of model indices, obtaining a cube of ≈225 000 individual models, with $-2.25 \leqslant Z \leqslant +0.67$, $0.1 \leqslant$ age $\leqslant 15$ Gyr and $-0.2 \leqslant$ [Mg/Fe] $\leqslant 0.5$. We then determined the model closest to our observations (the set of three indices) for each Voronoi bin in our galaxies, via a $\chi^2$ minimization technique, consisting in minimizing contemporaneously the distance between all of the observed and the model indices, weighted with the observational error on the line strengths (see Section 3.1 for the actual figures). We attributed to the galaxy bin the age, metallicity and abundance ratio of the selected model. The third row in Figs 6–14 shows the age, metallicity and abundance ratio maps obtained in this way. We are aware that it is an oversimplification to represent a galaxy's population using an SSP, however, we want to apply this method as a 'zero-order' estimate, before moving to somewhat more sophisticated ones. Fig. 19 plots against each other the age, metallicity and abundance ratio values calculated over the central aperture spectrum. Our sample galaxies are represented with black symbols. Overplotted with red symbols are the ellipticals and lenticular galaxies of the SAURON survey (Kuntschner et al., in preparation), while the blue symbols represent the early-type spirals of the SAURON survey (Paper XI). Despite the problems intrinsic to this approach, from this plot we can see that, as expected, our galaxies are on average younger and more metal-poor than early-type galaxies, and have on average a value of [Mg/Fe] closer to zero, ranging from slightly subsolar to slightly overabundant. This confirms what we saw in Fig. 16, where we noted that the late-type spirals were compatible with models with [Mg/Fe] = 0.

In order to assess the dependence of our results on the set of models used, we performed the following exercise. We took the model spectra from the SSP library of Vazdekis (1999) and calculated the line-strength indices on them, obtaining a grid of 322 model indices. Then we determined, galaxy by galaxy, the model that best matched our observations, deriving age and metallicity estimates. Abundance ratios are fixed to solar values in the library of Vazdekis (1999). In Fig. 20, we plot against each other the ages and metallicities obtained for the central 1.5-arcsec apertures of our galaxies using the Thomas (horizontal axis) and the Vazdekis (vertical axis) models. Overplotted with solid lines are the 1:1 relations. We see that there are no dramatic differences between the two sets of measurements, though the Vazdekis models tend in several cases

[5] http://astro.u-strasbg.fr/Obs/GALAXIES/stecmap_eng.html.

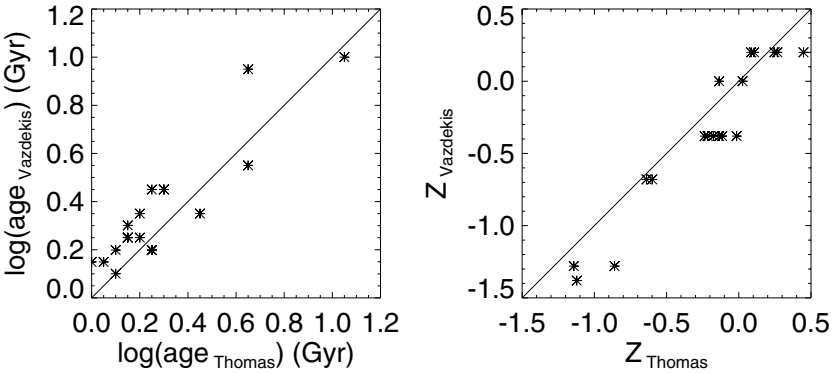


**Figure 20.** Comparison between the ages (left-hand panel, in Gyr) and metallicities (right-hand panel) obtained from our one-SSP approach using the models of Thomas et al. (2003) (horizontal axis, limited to nearly solar abundance ratios) and Vazdekis (1999) (vertical axis). The solid lines overplotted represent the 1:1 relation.

to predict slightly older ages and lower metallicities with respect to the Thomas ones. The small residual differences do not depend on the fixed abundance ratios of the Vazdekis models: the ages and metallicities on the horizontal axis in Fig. 20 are obtained for this test considering only the Thomas models closest to solar abundance ratios. The differences in the metallicity could be instead at least partially due to the coarseness in $Z$ of the model grid obtained from the Vazdekis models.

As also noted in Paper XI, in some cases an unconstrained SSP fit cannot provide a suitable representation of a galaxy. In the case of a complex star formation history, which cannot be approximated by a single, instantaneous burst, the SSP-equivalent parameters must be interpreted with caution, as a 'zero-order' estimate, as we already stressed. As an example, we remind the reader the case of the star formation ring in NGC 4321 discussed by Allard et al. (2006). They show that in the ring the line strength indices suggest the superposition of two components: a young stellar population and an old and metal-rich one. When they force a single SSP, they obtain low metallicity and old age. But it is known (Zaritsky et al. 1994) that the H II regions of this galaxy have supersolar metallicity: the one-SSP solution obtained by Allard et al. (2006) represents therefore an inconsistent description. As clearly visible from the first panel in Fig. 19, some of our galaxies also populate the region of the (metallicity, age) plane characterized by low metallicities (below $-1.0$) and old ages (above 10 Gyr). This is the case for the central aperture of NGC 864, for which our $\chi^2$ technique selects a model with $Z \approx -1.14$ and age $\approx 11$ Gyr. The line strength maps for this object (see Fig. 7) show that in the very centre the Fe5015 and Mg$b$ indices assume low values, and so does H$\beta$, on a large inner region. The low indices drive the metal-poor old population, but an SSP description might be too unrealistic for this object.

More generally, if, for example, a galaxy has undergone two separate bursts of star formation, the SSP-equivalent age will be biased towards the age of the youngest stars, and the SSP-equivalent metallicity will be biased towards the metallicity of the old population, as studied and described in detail by Serra & Trager (2007).

In order to put some physically motivated constraints to our one-SSP analysis, we decided to constrain the metallicity of our objects in a narrow range around the value in the model grid closest to the one determined from a relation between central stellar velocity dispersion and metallicity for early-type galaxies. In practice, we aim to apply a scaling relation obtained for spheroids (ellipticals and lenticulars). Our late-type galaxies do not host relevant bulge components (Ganda et al., in preparation), so the regions that we probe with our data do not fall under this category. Also, unlike for spheroids, $\sigma$ is not a good mass indicator in disc galaxies. But in any case, using a '$\sigma$ relation' for spheroids is a 'zero-order' approach to extrapolate the metal content of the old stars in low-mass galaxies. We investigated several possibilities for a metallicity–$\sigma$ relation for early-type galaxies. The resulting relations can differ from each other significantly, particularly at the low-$\sigma$ end, because of differences in the methods, in the models used, and in the underlying assumptions.

A possible and common way is to go through stellar population models, estimate the ages and metallicities by comparison of observations and SSP models, and then fit a relation with $\sigma$. This approach has been extensively investigated in the literature; we will refer to it as ' the model approach'. As a prototype, we refer to the work of Thomas et al. (2005), who studied 124 early-type galaxies in high- and low-density environments and derived their ages, metallicities and element ratios. For the galaxies in high-density environments, they retrieved the following relation:

$$Z = 0.55 \log(\sigma) - 1.06. \quad (6)$$

See also Kuntschner (2000) for a similar result.

Another possibility, to which we will refer as 'the index–$\sigma$ approach', is to assume a set of index–$\sigma$ relations for early-type galaxies, extrapolate them to the range of $\sigma$ under investigation, from the measured $\sigma$ infer the indices and from these, via a comparison with models, an estimate for the metallicity. In practice, we used the H$\beta'-\sigma$, Fe5015$'-\sigma$, Mg$b'-\sigma$ relations published in Paper VI for the 48 ellipticals and lenticulars of the main SAURON survey. Using these relations and the measured values for the central aperture velocity dispersions of our galaxies, we obtained a set of index values. We then compared them with the models of Thomas et al. (2003) via the previously described $\chi^2$ minimization, but choosing only among models with solar abundance ratios and age $\approx$12.6 Gyr. In this way we come to the estimate of the metallicity of an old spheroid at the observed velocity dispersion. We will adopt the estimates obtained in this way to put a constraint on the metallicity.

Another approach, which does not involve any stellar population modelling, relies on empirical calibrations and tight observed scaling relations between metal indices and velocity dispersion. Consider the $Mg_2-\sigma$ relation for elliptical and lenticular galaxies given by Jørgensen et al. (1996) (equation 3). If we combine this relation with the $Mg_2$–metallicity calibration from Buzzoni, Gariboldi

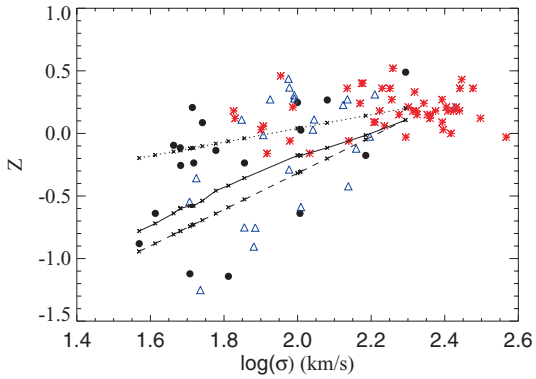


**Figure 21.** Relation between central metallicity and central velocity dispersion (in decimal logarithm and units of km $s^{-1}$) for the E and S0 galaxies (Kuntschner et al., in preparation, red symbols) and the Sa (Paper XI, blue symbols) of the SAURON survey and for our late-type spirals (black dots), from our one-SSP analysis. The overplotted lines represent the relation metallicity–velocity dispersion obtained in different ways, drawn on the $\sigma$ range of our data only: the dotted line reproduces equation (6) ('model approach'), the dashed line equation (8) ('empirical approach') and the solid lines represent a relation based on the assumption of a set of index–$\sigma$ relations. See text for a more complete description.

& Mantegazza (1992)[6]:

$$\mathrm{Mg}_2 = 0.135Z + 0.28, \tag{7}$$

we obtain a relation between metallicity and velocity dispersion, holding for early-type galaxies[7]:

$$Z = 1.452\log(\sigma) - 3.222. \tag{8}$$

We call this last approach 'the empirical approach'.

In Fig. 21 we show in the ($\log(\sigma)$, $Z$) plane the distribution of the elliptical and lenticular galaxies in the SAURON survey (red symbols, from Kuntschner et al., in preparation), the Sa galaxies from the same survey (blue symbols, from Paper XI), together with our own galaxies (black dots). All the values refer to the central apertures, and the metallicities are obtained from the one-SSP analysis. The lines overplotted in the figure represent the various metallicity–velocity dispersion relations for E/S0 galaxies described above. The dotted line reproduces equation (6) (from 'the model approach'), the dashed line equation (8) (from 'the empirical approach') and the solid line connects the points representing our galaxies in the ($\log(\sigma)$, $Z$) plane according to 'the index–$\sigma$' approach, the second one we presented.

We re-evaluated our age estimates by imposing a constraint on the metallicity, allowing it to vary only in a narrow range ($\pm$0.1 dex) around the metallicity given, galaxy by galaxy, by the solid black line in Fig. 21 ('the index–$\sigma$ approach' discussed above). We preferred this approach to the other two because it is based on empirical relations, and does not rely exclusively on models, unlike 'the model approach', and because it uses more than just magnesium to establish the metallicity of the old population, contrary to 'the empirical approach'. Fig. 22 is equivalent to Fig. 19, but with the constraints on metallicity. In Fig. 23 we plot the constrained ages against the unconstrained ones: we can note that for very young ages the values are close, and differ more and more going to older ages. The fact that in some cases the constrained age differs from the unconstrained might indicate either that the imposed metallicity is inappropriate or that the one-SSP assumption is wrong, and the galaxy's star formation history cannot be approximated by an instantaneous burst.

In Table 5 we list the population parameters measured, both in the unconstrained and in the constrained case, on the central aperture of our galaxies.

### 6.2 Two-population analysis

A galaxy is most likely characterized by stellar populations that are more complex than SSPs; therefore, in order to try to build a more realistic picture of our galaxies, we investigated more sophisticated approaches. As an attempt, we explored a two-SSP scenario, describing the galaxy as the superposition of an old population and a younger one. In practice, we want to describe the galaxy population as

$$\mathrm{pop\_tot} = (1 - f) \times \mathrm{pop\_old} + f \times \mathrm{pop\_young}, \tag{9}$$

where pop_old is an $\approx$12.6-Gyr-old SSP with metallicity fixed to the value close to the one obtained from the $Z$–$\sigma$ relation (on the basis of what we called 'the index–$\sigma$ approach') and pop_young is an SSP with age below 5 Gyr and free metallicity; the limit of 5 Gyr was chosen in order to have a population younger than the old component, but at the same time not limited to very young ages; $f$ is the mass fraction of the young component and varies between 0 and 1. To do this, we take the model spectra from Vazdekis (1999) and select, galaxy by galaxy, the 12.6-Gyr-old model with the metallicity closest to the one given by the solid line in Fig. 21, among those available in the model grid, and combine it with all the other SSP models in the library, with varying mass fractions. In this way we obtain for each galaxy a set of 6762 'composite model spectra', with varying age and metallicity of the young component and relative mass fraction. On these spectra we compute the line strength indices, obtaining for each galaxy a grid of 'composite model indices'. Since we use the model library of Vazdekis (1999), the abundance ratio is fixed to solar values, which for our objects is a quite fair approximation, as we saw in the previous section. We then use the same $\chi^2$ technique as for the one-SSP analysis and determine, spectrum by spectrum, the composite model closest to our observed line strengths. This gives us an estimate for the age and metallicity of the young component and its mass fraction.

Fig. 24 plots against each other the parameters fitted on the spectrum averaged in a central aperture of 1.5 arcsec radius. We see that the young component spans a range in age from below 1 to $\approx$4.5 Gyr, a range in $Z$ from $-1.38$ to $+0.2$ and that its mass contribution to the global galaxy population $f$ varies from $\approx$10 per cent (NGC 2805) to $\approx$95 per cent (NGC 1042, 2964, 3949, 4487).

The main problem of this approach is the degeneracy of the parameter space, which must act as a warning for the reader against the robustness of the ages and mass fraction estimates for the young component presented in Fig. 24. This degeneracy is illustrated in Figs 25 and 26. In Fig. 25, we plot, for different choices of the metallicity of the old component and solar metallicity for the young one, the points representing the models in the ([MgFe50], H$\beta$) diagram. Different colours represent different weights of the young

[6] These authors calibrate the dependence of $\mathrm{Mg}_2$ from stellar parameters using an observed stellar library and find a general relation, that reduces to the one reported here (equation 7) in the parameter range spanned by elliptical galaxies.

[7] We warn the reader about the fact that the $\mathrm{Mg}_2$ index has a slightly different definition in the papers of Jørgensen et al. (1996) and Buzzoni et al. (1992), and that we have not taken this difference into account in deriving equation (8).

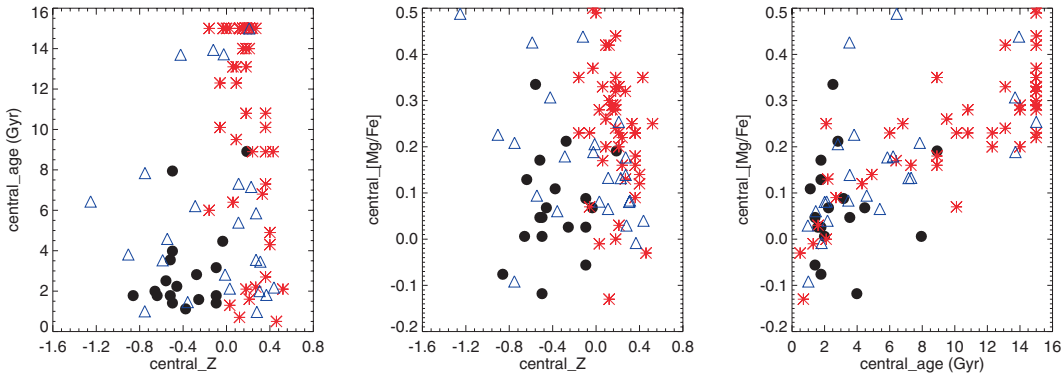


**Figure 22.** Same plots as in Fig. 19, but referring to the case with constrained metallicity (see text in Section 6.1 for more details), for our late-type spirals (black symbols); for the E/S0 (red symbols) and the Sa (blue symbols) galaxies no constraint on metallicity is applied.

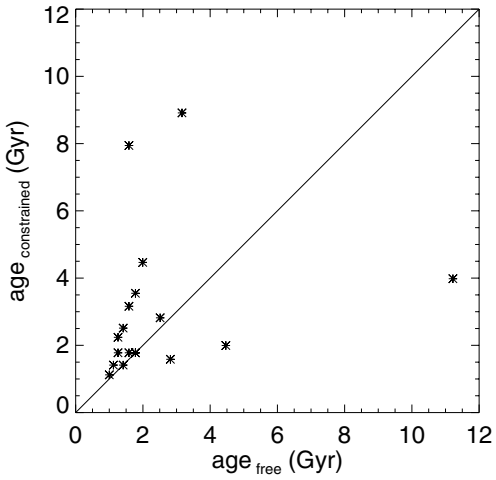


**Figure 23.** Constrained ($y$-axis) versus unconstrained ($x$-axis) age (in Gyr), measured on the central apertures of our galaxies with the one-SSP approach.

component in the composite models, from 0.1 (black) to 0.9 (light green). From these plots it is evident that it is not possible to significantly discriminate the effects of age and mass fraction of the young component. Fig. 26 shows the projection of the $\Delta\chi^2$ space (metallicity, age and mass fraction of the young component) on the (age, fraction) plane and the contours representing the 1, 2, 3$\sigma$ confidence level, based on the $\Delta\chi^2$ for two degree of freedom, for the central aperture of some of the galaxies. We see that very large regions of the parameter space are equivalent in terms of $\chi^2$, and that even in cases where the age is rather well constrained (see NGC 2805), the mass fraction is badly determined. Therefore, we see that we cannot extract solid conclusions from this method, despite its interesting principle, and we decided not to push it further and not to present the two-dimensional maps of the inferred parameters.

### 6.3 Continuous star formation

'The star formation history of galaxies is imprinted in their integrated light', state Bruzual & Charlot (2003) in a paper where they present a new model for the spectral evolution of stellar populations at ages between $1 \times 10^4$ and $2 \times 10^{10}$ yr for a range of metallicities (Bruzual & Charlot 2003). In practice, they use the *isochrone synthesis* technique to compute the spectral evolution of stellar populations. This technique relies on the fact that any stellar population

**Table 5.** Population parameters from our one-SSP analysis. The subscript 'c' refers to the quantities obtained in the case where we constrain the metallicity within a narrow range (±0.1 dex) around the metallicity given by the $Z-\sigma$ relation. Age is in Gyr and metallicity in decimal logarithm, with solar metallicity as zero-point.

| NGC | Age | Age$_c$ | $Z$ | $Z_c$ | [Mg/Fe] | [Mg/Fe]$_c$ |
|---|---|---|---|---|---|---|
| 488 | 3.162 | 8.913 | 0.489 | 0.187 | 0.191 | 0.191 |
| 628 | 1.585 | 7.943 | 0.207 | −0.498 | −0.118 | 0.006 |
| 772 | 1.995 | 4.467 | 0.267 | −0.035 | 0.068 | 0.068 |
| 864 | 11.220 | 3.981 | −1.142 | −0.498 | −0.015 | −0.118 |
| 1042 | 1.259 | 2.239 | 0.086 | −0.458 | −0.076 | 0.068 |
| 2805 | 1.413 | 2.512 | −0.095 | −0.558 | 0.191 | 0.335 |
| 2964 | 2.818 | 1.585 | −0.639 | −0.256 | 0.068 | 0.026 |
| 3346 | 1.259 | 1.778 | −0.256 | −0.518 | 0.109 | 0.171 |
| 3423 | 1.778 | 3.548 | −0.115 | −0.518 | −0.035 | 0.047 |
| 3949 | 1.000 | 1.122 | −0.136 | −0.377 | 0.006 | 0.109 |
| 4030 | 1.585 | 3.162 | 0.247 | −0.095 | 0.047 | 0.088 |
| 4102 | 1.413 | 1.413 | − 0.176 | −0.095 | −0.015 | −0.056 |
| 4254 | 2.512 | 2.818 | −0.236 | −0.276 | 0.171 | 0.212 |
| 4487 | 4.467 | 1.995 | −1.122 | −0.659 | 0.047 | 0.006 |
| 4775 | 1.778 | 1.778 | −0.639 | −0.639 | 0.129 | 0.129 |
| 5585 | 1.778 | 1.778 | −0.881 | −0.860 | − 0.076 | −0.076 |
| 5668 | 1.122 | 1.413 | −0.236 | −0.498 | −0.015 | 0.047 |
| 5678 | 1.585 | 1.778 | 0.026 | −0.095 | −0.015 | 0.026 |

can be expanded in a series of instantaneous starbursts or SSPs. So, the spectral energy distribution at time $t$ of a stellar population can be written as in equation (1) in Bruzual & Charlot (2003):

$$F_\lambda(t) = \int_0^t \psi(t-t')S_\lambda[t', \zeta(t-t')]\,\mathrm{d}t', \qquad (10)$$

where $\psi(t)$ and $\zeta(t)$ are, respectively, the SFR and the metal-enrichment law, as a function of time, and $S_\lambda[t', \zeta(t-t')]$ is the power radiated by an SSP of age $t'$ and metallicity $\zeta(t-t')$ per unit wavelength and unit initial mass. Bruzual & Charlot (2003) compute their models with various choices for the initial mass function (IMF), the metallicity of the initial SSP and the stellar evolution prescription. They also provide as online material some tools that allow the user to compute the spectral evolution – in time – of an SSP for different star formation history scenarios.[8] We chose to use these tools in order to apply an evolutionary analysis to our data.

[8] The program we used are available from the web page http://www.cida.ve/∼bruzual/bc2003.

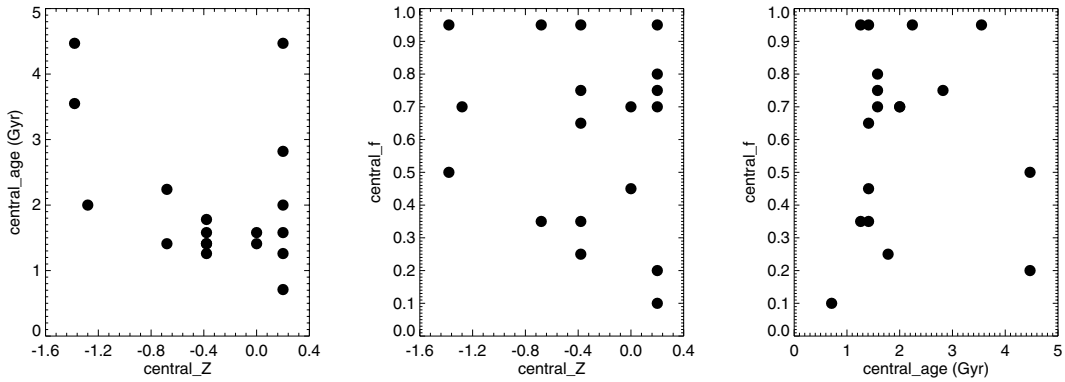


**Figure 24.** Fitted parameters from our two-SSP analysis, measured on the central apertures. In the left-hand panel we have the age (in Gyr) against the metallicity (in decimal logarithm, with the solar metallicity as zero-point) of the young component pop_young; in the middle its mass fraction against its metallicity; in the right-hand panel, the mass fraction of the young component against its age.

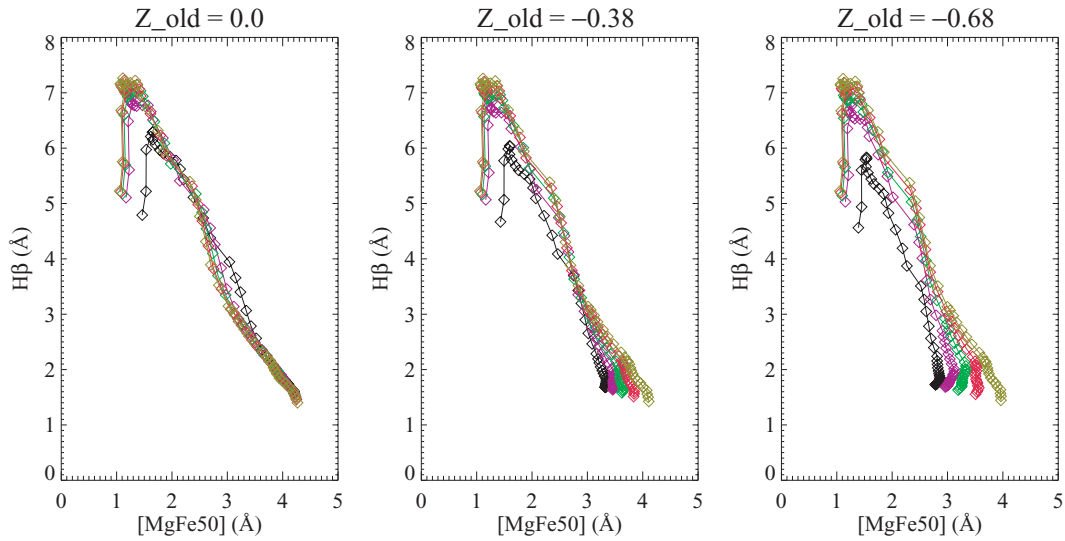


**Figure 25.** Composite models for different choices of the metallicity of the old component (indicated at the top of each panel) and solar metallicity of the young one represented by points in the ([MgFe50], H$\beta$) plane. Different colours refer to different values of the mass fraction of the young component in the composite model. The effects of age and fraction of the young component on the line strength indices of the composite models are degenerate.

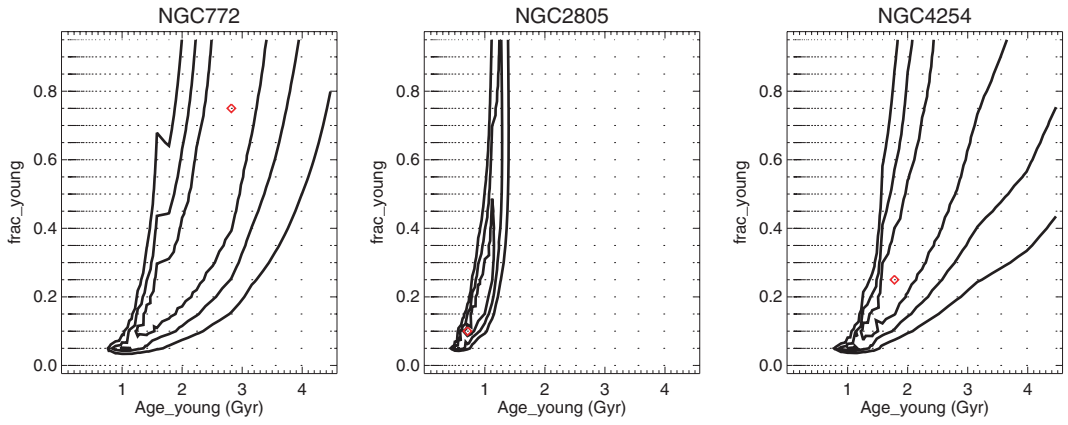


**Figure 26.** Contours of $\Delta\chi^2$ projected on the plane (age, fraction) of the young component at the 1, 2, 3$\sigma$ confidence level, for the central apertures of NGC 772, 2805, 4254; the red symbol marks the best-fitting model. These plots clearly show that the two-SSP approach is unable to constrain the fitted parameters, and that age and mass fraction of the young component are degenerate.

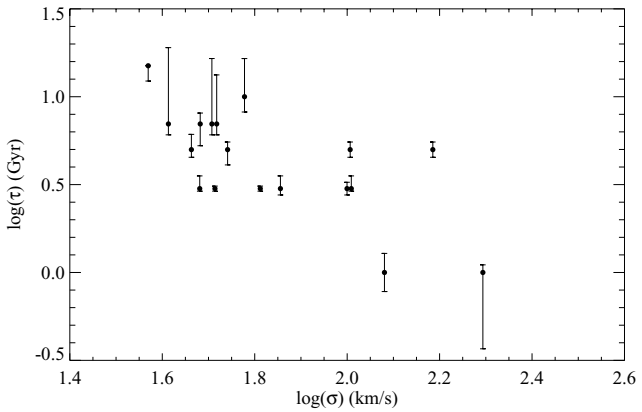


**Figure 27.** Central aperture values for the e-folding time-scale $\tau$ against central velocity dispersion $\sigma$ (both in units of decimal logarithm), in an exponentially declining star formation scenario; the $\tau$ values are obtained selecting among models with age = 10 Gyr and $\epsilon = 1$; the error bars come from a rough estimate on the basis of the $1\sigma$ contour plots of the projection of $\Delta\chi^2$ on the $\tau$–metallicity plane.

Starting from the SSP models from Bruzual & Charlot (2003) obtained using the Chabrier (2003) IMF, for different choices of the initial metallicity (viz. $Z = -1.69$, $-0.69$, $-0.39$, 0.0, 0.39), we computed the time evolution with constant and with exponentially declining SFR: respectively, $\psi(t) =$ constant and $\psi(t) = [1\,\mathrm{M}_\odot + \epsilon M_{\mathrm{PG}}(t)]\,\tau^{-1}\,\exp(-t/\tau)$, where $\tau$ is the e-folding time-scale and $M_{\mathrm{PG}}(t)$ is the mass of gas processed into stars and re-ejected into the interstellar medium at the time $t$; the parameter $\epsilon$ sets the fraction of the ejected gas that is re-used in new star formation episodes; we only explored the cases $\epsilon = 0$ (no recycling) and $\epsilon = 1$ (all of the ejecta go into new stars). In any case, the actual value of $\epsilon$ does not change our results significantly. These are both plausible scenarios: the constant star formation history has long been considered as a suitable scenario for spirals: 'star formation has proceeded at relatively constant rate over the lifetimes of most late-type spiral galaxies' (Kennicutt 1983), while the exponentially declining star formation describes the situation of a starburst of duration $\tau$; we note that the case $\tau \to \infty$ approximates the constant star formation scenario, while the case $\tau \to 0$ reproduces an instantaneous burst or SSP. We computed the spectral evolution for the chosen metallicities, for both cases $\epsilon = 0$ and $\epsilon = 1$ and for several choices of $\tau$: $\tau$ = 0.5, 1.0, 3.0, 5.0, 7.0, 10.0, 12.0 and 15.0 Gyr. The tools provided by Bruzual & Charlot (2003) also include an option for computing the effect of attenuation by dust, but we decided not to use this possibility, in order not to further increase the number of parameters at play.

For all of the selected cases we calculated the time evolution of the Lick indices using the programs from Bruzual & Charlot (2003) and focused on the situation at $t = 10$ Gyr, building a model grid of Lick indices for different metallicities, $\tau$ and $\epsilon$ (0 or 1) and age fixed at 10 Gyr and then compared them with the line strength indices of the SAURON spectra, via the $\chi^2$ minimization technique used also in the previous sections. In this way, we come to an estimate for the time-scale $\tau$, $\epsilon$ and the metallicity. Fixing the age to 10 Gyr is equivalent to assume that the galaxy existed for 10 Gyr, and to try to describe how stars were formed over that time. We tested that the fitted parameters ($\tau$ and metallicity) had negligible variations when fixing the value of $\epsilon$, therefore we repeated our estimates allowing only models with $\epsilon = 1$ and will refer to this case from now on.

In Figs 6–14, the top right-hand panel shows, galaxy by galaxy, the two-dimensional maps of $\tau$, obtained for the exponentially declining SFR, for age fixed to 10 Gyr and $\epsilon = 1$. Interesting features of the individual $\tau$ maps, whenever present, are highlighted in Appendix B. As for the metallicity maps, obtained in the $\chi^2$ minimization and not shown in this paper, we can state that in the majority of cases they resemble in their structure the metallicity maps obtained in the one-SSP approach; the actual numbers are different, since the models used in the two approaches are different and also the metallicity ranges and values explored by the model grids differ, but the spatial structure is generally similar.

If we focus on the values obtained for the central apertures, we find a correlation between the best-fitting $\tau$ and the central velocity dispersion, as shown in Fig. 27 where we plot $\log(\tau)$ against $\log(\sigma)$. We see that higher $\sigma$ galaxies, which are larger and more massive, tend to have shorter star formation time-scales, more consistent with an instantaneous burst scenario, while at the low-$\sigma$ end the smaller galaxies tend to have larger $\tau$, indicating a star formation history spread over time. Therefore, the time-scale $\tau$ represents a physically meaningful parameter, parametrizing a smooth transition from SSP-like to constant SFR.

Fig. 28 shows that rather tight correlations exist also between the central $\tau$ and the central line strength indices. These plots tell us that old, metal-rich galaxies (low H$\beta$, high Fe5015 and Mg$b$ values) have shorter star formation time-scales, while young and

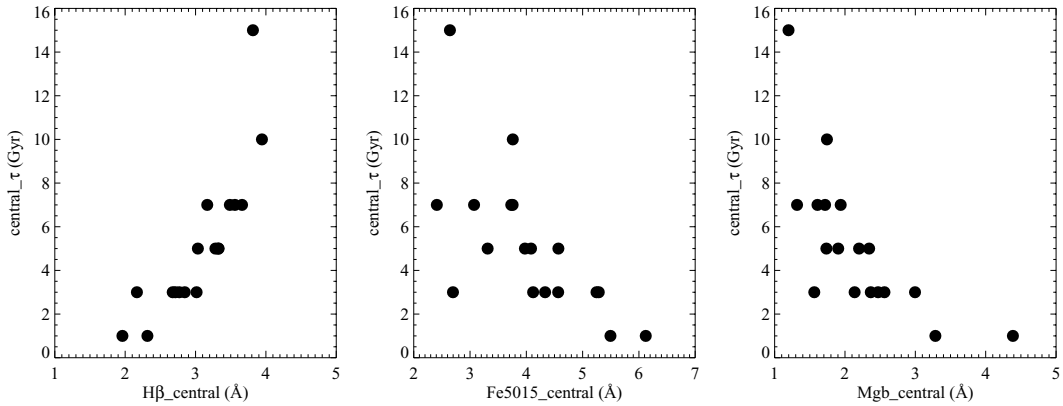


**Figure 28.** Central aperture values for the e-folding time-scale $\tau$ (in Gyr) of an exponentially declining star formation history, against the central line strength indices (expressed in Å): H$\beta$ in the left-hand panel, Fe5015 in the middle and Mg$b$ in the right-hand panel; the $\tau$ values are obtained selecting, in the fit, among models with age = 10 Gyr and $\epsilon = 1$ (see text for details).

**Table 6.** Best-fitting values for the star formation time-scale $\tau$ (in Gyr) measured on the central apertures of our galaxies, obtained for the choices age = 10 Gyr and $\epsilon = 1$, in an exponentially declining SFR scenario.

| NGC | $\tau$ | NGC | $\tau$ | NGC | $\tau$ |
|---|---|---|---|---|---|
| 488 | 1 | 2964 | 5 | 4254 | 3 |
| 628 | 3 | 3346 | 7 | 4487 | 7 |
| 772 | 1 | 3423 | 3 | 4775 | 7 |
| 864 | 3 | 3949 | 10 | 5585 | 15 |
| 1042 | 5 | 4030 | 3 | 5668 | 7 |
| 2805 | 5 | 4102 | 5 | 5678 | 3 |

more metal-poor galaxies (higher H$\beta$, lower Fe5015 and Mg$b$) have a star formation history more extended in time: we find again a smooth transition between an SSP-like and constant star formation. The central aperture values of $\tau$ used in Figs 27 and 28 are listed in Table 6.

We also investigated the constant star formation history scenario, by selecting the corresponding option when using the programs from Bruzual & Charlot (2003), building a grid with the model indices for the exponentially declining SFR and adding those for constant SFR, for the various metallicity values selected and for $\epsilon = 1$ and age fixed to 10 Gyr. When applying our $\chi^2$ minimization procedure, we found that the constant star formation was preferred in the regions where the fit with the exponential star formation only had selected the highest values allowed for the time-scale $\tau$. This confirms our interpretation of $\tau$ as a parameter describing a continuous transition from constant SFR to SSP.

We then repeated the analysis for different values of the fixed age of the evolved models, spanning the range 1–18 Gyr and found that the $\tau$ values depend on the fixed age, given the existence of a strong degeneracy between age and $\tau$, while the metallicities are more robust.

The main interpretative difficulty of this method is indeed due to the degeneracies in the parameter space, which are difficult to break with the few observed Lick indices that we measure. Nevertheless, by inspecting the contours of $\Delta\chi^2$ in the $\tau$–metallicity plane, for several choices of the fixed age of the evolved models, we can in some cases exclude certain star formation scenarios in favour of others, even though we cannot give a precise, quantitative estimate of the fitted parameters. For example, in the case of NGC 488, if we look at the two-dimensional $\Delta\chi^2$ space (metallicity, $\tau$), for a fixed age of the evolved models), and look at the contours in the $\tau$–metallicity plane representing the $3\sigma$ confidence level, based on the $\Delta\chi^2$ for one degree of freedom, we note that it lies in a region far from the high-$\tau$ end, and this happens independently on the chosen values of the fixed age. Even if we perform the minimization by allowing free age, $\tau$ and metallicity, and examine the projection of the $\Delta\chi^2$ contours in the $\tau$–age plane, we see that for all ages we can exclude large $\tau$ values at a high confidence level. This must be regarded as an exercise, since we are not interested in fitting simultaneously age and $\tau$, but it gives us insight on the impact of the degeneracies and of our assumptions on the robustness of our conclusions. Thus, for NGC 488 we can safely state that we can exclude a constant star formation scenario in favour of an exponentially declining SFR, with a short time-scale $\tau$ (closer to an instantaneous burst than to a constant SFR). This is illustrated in the first column in Fig. 29. Similar hints for the star formation history of other galaxies will be given, whenever possible, in Appendix B, dedicated to the description of the single galaxies individually. For all galaxies, the $\Delta\chi^2$ contours for the fit at different fixed ages and with free age are presented in Figs 29–31.

## 7 SUMMARY

In this paper we presented the first integral-field measurements of line strength indices and stellar population parameters for a sample of late-type spiral galaxies. This work is based on data of 18 spirals spanning a range in type between Sb and Sd, observed with SAURON, which provides measurements of the Lick indices H$\beta$, Fe5015 and Mg$b$ over an FoV covering the nuclear region of our objects.

Here we summarize the main achievements of the paper.

(i) We presented the two-dimensional maps of the line strength indices and analysed the values extracted on a central aperture of 1.5 arcsec radius.

(ii) We looked at the relations with morphological type: we found that late-type spirals do differ from earlier type galaxies in terms of their populations, having globally higher H$\beta$ values and lower metal indices than ellipticals, lenticulars and early-type spirals. This suggests younger ages and lower metallicities.

(iii) We investigated the relations between indices and central velocity dispersion: late-type spirals do not obey the index–$\sigma$ relations found for early-type galaxies: our galaxies lie above the H$\beta-\sigma$ and below the Mg$b-\sigma$ relations determined for the elliptical galaxies, that correspond to old populations.

(iv) We determined SSP-equivalent ages, metallicities and abundance ratios by comparison of our observed indices with models: ages are mainly young, metallicities low and abundance ratios close to solar; the range spanned in the parameters is narrower than for early-type spirals.

(v) We investigated the possibility of recovering the star formation history: we assumed that the galaxies formed 10 Gyr ago, and that they experienced an exponentially declining or constant SFR since then, and compared our indices with the evolved models of Bruzual & Charlot (2003); the fit returned an estimate for the e-folding time-scale for star formation $\tau$, which parametrizes a smooth transition from an SSP-like star formation history to a constant SFR: small $\tau$ approximate an instantaneous burst and very large $\tau$ reproduce a constant SFR; for the central apertures of our galaxies, we found a large range in $\tau$ values, from 1 to 15 Gyr, covering basically the whole parameter interval that we explored.

(vi) Interestingly, we found a trend between the fitted $\tau$ and the central velocity dispersion, in the sense that galaxies with large $\sigma$ tend to have small $\tau$ and galaxies with low $\sigma$ tend to have large $\tau$.

Our observations and results nicely fit in the scenario summarized by Kennicutt (1998): there are two modes of star formation; one takes place in the extended discs of spiral and irregular galaxies, the other in compact gas discs in the nuclear regions of galaxies. The first has been detected mainly via H$\alpha$ surveys and it is strongly dependent on the morphological type: the SFR increases by a factor of $\approx$20 going from Sa to Sc galaxies. Similar information is derived from observations of the ultraviolet (UV) continuum and broad-band visible colours. The second mode of star formation can be found in the circumnuclear regions; the physical conditions in these regions are in many cases distinct from the more extended star-forming discs. The circumnuclear star formation is characterized by the absolute range in SFR, much higher spatial concentration of gas and stars and its burst-like nature (Kennicutt 1998). Circumnuclear star formation is largely decoupled from Hubble type. Studies on the dependence of nuclear H$\alpha$ emission in star-forming nuclei as a function of galaxy type (Stauffer 1982; Keel 1983; Ho et al. 1997) showed that the detection frequency of H II region nuclei is a

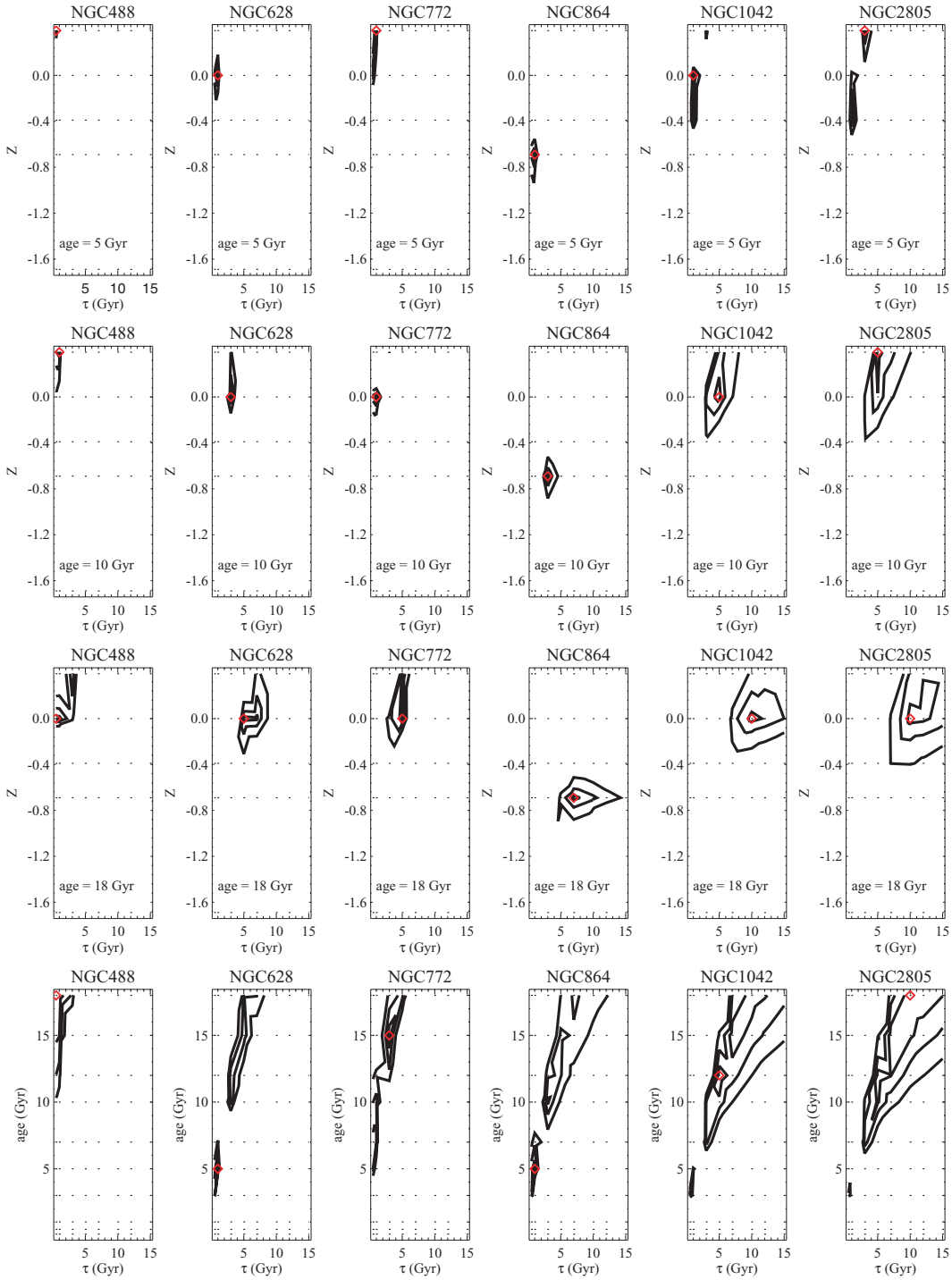


**Figure 29.** First column: projections of the 1, 2 and $3\sigma\,\Delta\chi^2$ contours on the $\tau$–metallicity plane for the central aperture of NGC 488, for different fixed ages in the fit (5 Gyr, first row; 10 Gyr, second row; 18 Gyr, third row); projections of the 1, 2 and $3\sigma\,\Delta\chi^2$ contours on the $\tau$–age plane for the central aperture of NGC 488, for the fit performed with free age, $\tau$ and metallicity, fourth row. Second to fifth columns: as in the first column, but for NGC 628, 772, 864, 1042 and 2805; in all plots, the red symbol indicates the best-fitting model. These plots demonstrate that for NGC 488, 628 and 772 we can exclude at a high confidence level a constant star formation scenario, while, for example, for NGC 2805 high values of $\tau$ are not highly unlikely at all ages.

monotonic function of type, increasing from 0 per cent in elliptical galaxies to 8 per cent in S0, 22 per cent in Sa, 51 per cent in Sb and 80 per cent in Sc–Im galaxies. Among the galaxies with nuclear star formation, the H$\alpha$ luminosities show the opposite trend; the average extinction-corrected luminosity of H II region nuclei in S0–Sbc galaxies is nine times higher than in Sc galaxies. The conclusion of these studies, as summarized by Kennicutt (1998), is that the bulk of the total nuclear star formation in galaxies is weighted towards

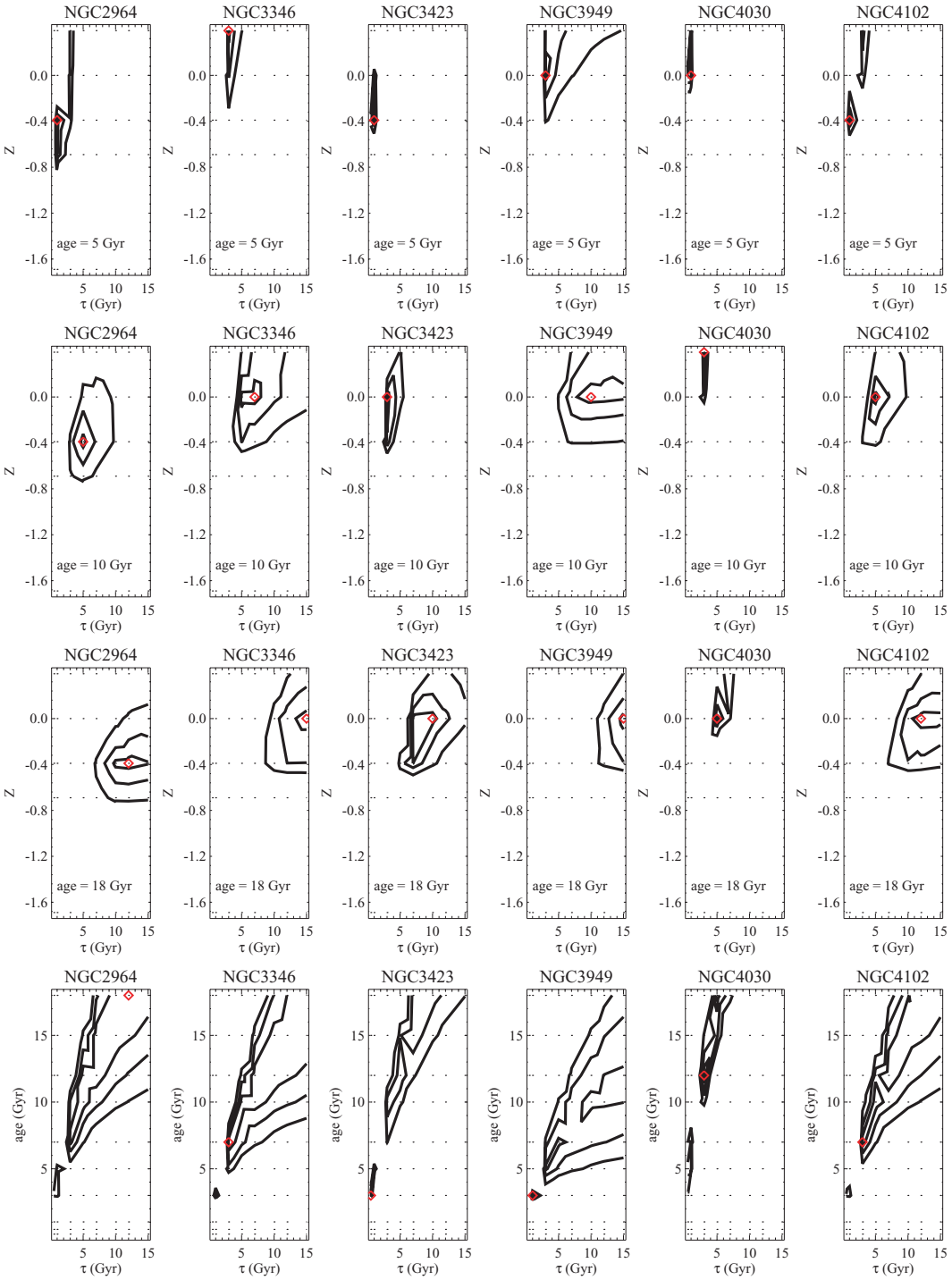


**Figure 30.** As in Fig. 29, but for NGC 2964, 3346, 3423, 3949, 4030 and 4102.

the earlier Hubble types, even though the frequency of occurrence is higher in the late-types. According to Kormendy & Kennicutt (2004), the central star formation accounts for 10–100 per cent of the total SFR of spiral galaxies. The highest fractions occur in early-type spiral galaxies, which typically have low SFRs in their outer discs (Kennicutt & Kent 1983).

The work presented in this paper supports this picture: if we put together the information gathered from the sample of E/S0s of Paper VI, the sample of Sa galaxies of Paper XI and our own sample, and look at the behaviour along the Hubble sequence, we find that early-type spirals show a larger range in age than both E/S0s and late-type spirals; this is consistent with a scenario where the star formation in elliptical and lenticular galaxies is not very important, in early-type spirals it is dominated by short bursts and in late-type galaxies it is more quiescent. This is also supported by our finding that big spirals tend to have an SSP-like star formation

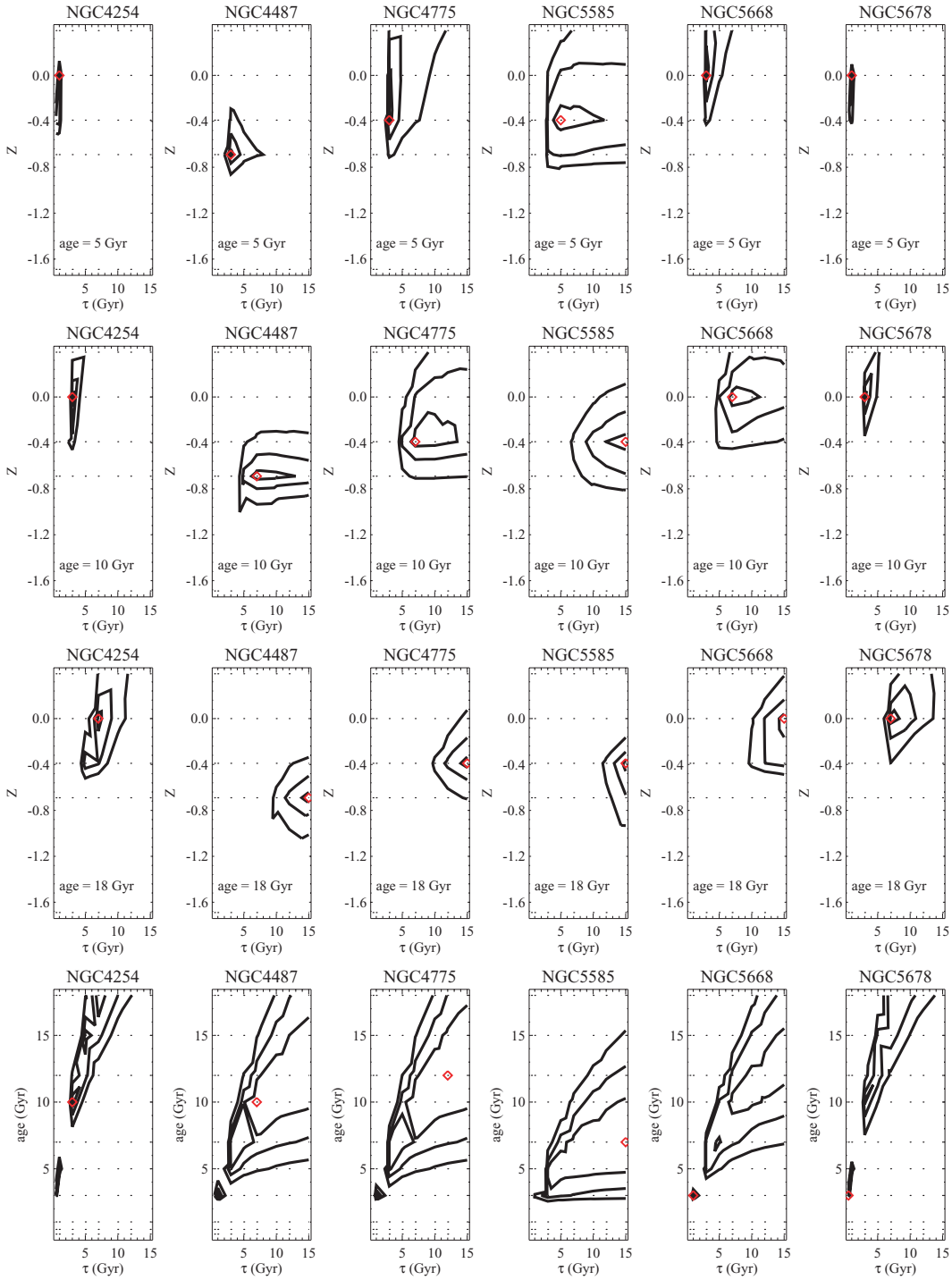


**Figure 31.** As in Fig. 29, but for NGC 4254, 4487, 4775, 5585, 5668 and 5678.

history, while for smaller ones the star formation history is better approximated by a constant over time.

The following steps in the analysis of the SAURON data here presented and discussed will be a full investigation of the spatial information, with a more detailed study of the radial profiles (here shown in Appendix A) and the gradients, and an interpretation of the connection between features in the line strength maps and in the morphological appearance. The interdependencies between the populations and the kinematical structures (Ganda et al. 2006) will also be examined.

The main limitation of our work is the degeneracy in the parameter space in the different approaches we investigated. Our analysis relies on three data points only (the line strength indices within the SAURON spectral range), which are too few to break the degeneracies and constrain the fitted parameters. Therefore, it is urgent to complement the data presented here with spectra with a broader

spectral coverage. Observations at other wavelengths – both shorter and longer – would help building a complete picture: both the UV and the NIR spectral regions can provide population indicators much less affected by the model degeneracies found in the optical. In addition, different subpopulations contribute to the integrated light in different spectral ranges, therefore a multiwavelength study would be a step forward towards a full understanding of the formation and evolution of our objects.

## ACKNOWLEDGMENTS

We kindly acknowledge Isabel Pérez for very useful discussion and comment. We thank the referee for interesting comments that improved the paper. The SAURON – related projects are made possible through grants 614.13.003 and 781.74.203 from ASTRON/NWO and financial contributions from the Institut National des Sciences de l'Univers, the Université Claude Bernard Lyon I, the universities of Durham, Leiden, Groningen and Oxford, the British Council, PPARC grant 'Extragalactic Astronomy & Cosmology at Durham 1998–2002' and the Netherlands Research School for Astronomy NOVA. KG acknowledges support for the Ubbo Emmius PhD programme of the University of Groningen. MC acknowledges support from a PPARC Advanced Fellowship (PP/D005574/1). GvdV acknowledges support provided by NASA through Hubble Fellowship grant HST-HF-01202.01-A awarded by the Space Telescope Science Institute, which is operated by the Association of Universities for Research in Astronomy, Inc., for NASA, under contract NAS 5-26555. This project made use of the HyperLeda and NED data bases.

## REFERENCES

Afanasiev V. L., Sil'chenko O. K., 2005, A&A, 429, 825
Allard E. L., Knapen J. H., Peletier R. F., Sarzi M., 2006, MNRAS, 371, 1087
Bacon R. et al., 2001, MNRAS, 326, 23 (Paper I)
Bender R., Burstein D., Faber S. M., 1993, ApJ, 411, 153
Bernardi M., Sheth R. K., Annis J., Burles S., 2003, AJ, 125, 1882
Böker T., Laine S., van der Marel R. P., Sarzi M., Rix H.-W., Ho L. C., Shields J. C., 2001, A&AS, 199, 705
Böker T., Laine S., van der Marel R. P., Sarzi M., Rix H.-W., Ho L. C., Shields J. C., 2002, AJ, 123, 1389
Bosma A., Casini C., Heidmann H., van der Hulst J. M., van Woerden H., 1980, A&A, 89, 345
Bruzual C., Charlot S., 2003, MNRAS, 344, 1000
Burstein D., Davies R. L., Dressler A., Faber S. M., Lynden-Bell D., 1988, in Kron R. G., Renzini A., eds, ASSL Vol. 141, Towards Understanding Galaxies at High Redshift. Kluwer, Dordrecht, p. 17
Buzzoni A., Gariboldi G., Mantegazza L., 1992, AJ, 103, 1814
Cappellari M., Copin Y., 2003, MNRAS, 342, 345
Cappellari M., Emsellem E., 2004, PASP, 116, 138
Carollo C. M., 1999, ApJ, 523, 566
Carollo C. M., Stiavelli M., 1998, AJ, 115, 2306
Carollo C. M., Danziger I. J., Buson L., 1993, MNRAS, 265, 553
Carollo C. M., Stiavelli M., de Zeeuw P. T., Mack J., 1997, AJ, 114, 2366
Carollo C. M., Stiavelli M., Mack J., 1998, AJ, 116, 68
Carollo C. M., Stiavelli M., Seigar M., de Zeeuw P. T., Dejonghe H., 2002, AJ, 123, 159
Carollo C. M., Scarlata C., Stiavelli M., Wyse R. F. G., Mayer L., 2007, ApJ, 658, 960
Chabrier G., 2003, PASP, 115, 763
Cid Fernandes R. et al., 2004, ApJ, 605, 105
Cid Fernandes R., Gonzalez Delgado R. M., Storchi-Bergmann T., Martins L. P., Schmitt H., 2005, MNRAS, 356, 270
Colless M., Burstein D., Davies R. L., McMahan R. K., Saglia R. P., Wegner G., 1999, MNRAS, 303, 813
Condon J. J., Condon M. A., Grisler G., Puscell J. J., 1982, ApJ, 252, 102
Cornett R. H. et al., 1994, ApJ, 426, 553
Davies R. L., Sadler E. M., Peletier R. F., 1993, MNRAS, 315, 650
Denicoló G., Terlevich R., Terlevich E., Forbes D. A., Terlevich A., Carrasco L., 2005, MNRAS, 356, 1440
de Vaucouleurs G., de Vaucouleurs A., Corwin H. G. Jr, Buta R. J., Paturel G., Fouqué P., 1991, Third Reference Catalogue of Bright Galaxies. Springer-Verlag, New York (RC3)
de Zeeuw P. T. et al., 2002, MNRAS, 329, 513 (Paper II)
Devereux N. A., 1989, ApJ, 346, 126
Emsellem E. et al., 2004, MNRAS, 352, 721 (Paper III)
Espada D., Bosma A., Verdes-Montenegro L., Athanassoula E., Leon S., Sulentic J., Yun M. S., 2005, A&A, 442, 455
Faber S. M., Friel E. D., Burstein D., Gaskell C. M., 1985, ApJS, 57, 711
Falcón-Barroso J., 2003, PhD thesis, Univ. Nottingham
Falcón-Barroso J., Peletier R. F., Balcells M., 2002, MNRAS, 335, 741
Falcón-Barroso J. et al., 2006, MNRAS, 369, 529 (Paper VII)
Fisher D., Franx M., Illingworth G., 1995, ApJ, 448, 119
Fisher D., Franx M., Illingworth G., 1996, ApJ, 459, 110
Ganda K., Falcón-Barroso J., Peletier R. F., Cappellari M., Emsellem E., MCDermid R., de Zeeuw P. T., Caroll M., 2006, MNRAS, 367, 46
Gonzalez Delgado R. M., Cid Fernandes R., Perez E., Martins L. P., Storchi-Bergmann T., Schmitt H., Heckman T., Leitherer C., 2004, ApJ, 605, 127
Gorgas J., Faber S. M., Burstein D., Gonzalez J. J., Courteau S., Prosser C., 1993, ApJS, 86, 153
Ho L. C., Filippenko A. V., Sargent W. L. W., 1997, ApJ, 487, 579
Idiart T. P., de Freitas Pacheco J. A., Costa R. D. D., 1996, AJ, 112, 2541
Jablonka P., 2007, preprint (astro-ph/0701169)
Jablonka P., Martin P., Arimoto N., 1996, AJ, 112, 1415
Jørgensen I., 1999, MNRAS, 315, 607
Jørgensen I., Franx M., Kjæ rgaard P., 1996, MNRAS, 280, 167
Keel W. C., 1983, ApJ, 269, 466
Kennicutt R. C., 1983, ApJ, 272, 54
Kennicutt R. C., 1998, ARA&A, 36, 189
Kennicutt R. C., Kent S. M., 1983, AJ, 88, 1094
Kormendy J., Kennicutt R. C., 2004, ARA&A, 42, 603
Kuntschner H., 2000, MNRAS, 315, 184
Kuntschner H. et al., 2006, MNRAS, 369, 497 (Paper VI)
Laine S., Shlosman I., Knapen J. H., Peletier R. F., ApJ, 567, 92
Longhetti M., Rampazzo R., Bressan A., Chiosi C., 1998, A&AS, 315, 251
MacArthur L. A., Gonzalez J., Courteau S., 2007, in Peletier R. F., Vazdekis A., eds, Proc. IAU Symp. 241, Stellar Populations as Building Blocks of Galaxies, preprint (astro-ph/0701881)
Matthews L. D., Gallagher J. S., 2002, ApJS, 141, 492
McDermid R. M. et al., 2006, MNRAS, 373, 906 (Paper VIII)
Moorthy B. K., Holtzman J. A., 2006, MNRAS, 371, 583
Natali G., Pedichini F., Righini M., 1992, A&A, 256, 79
Noordermeer E., van der Hulst J. H., 2007, MNRAS, 376, 1480
Ocvirk P., Pichone C., Lançon A., Thiébaut E., 2006a, MNRAS, 365, 46
Ocvirk P., Pichone C., Lançon A., Thiébaut E., 2006b, MNRAS, 365, 74
Panter B., Heavens A. F., Jimenez R., 2003, MNRAS, 343, 1145
Peletier R. F. et al., 2007, preprint (astro-ph/07042839) (Paper XI)
Phookun B., Vogel S. N., Mundy L. G., 1993, ApJ, 418, 113
Proctor R. N., Sansom A. E., 2002, MNRAS, 333, 517
Reakes M., 1979, MNRAS, 187, 525
Rossa J., van der Marel R. P., Böker T., Gerssen J., Ho L. C., Rix H.-W., Shields J. C., Walcher C.-J., 2006, AJ, 132, 1074
Sánchez-Blázquez P., Gorgas J., Cardiel N., González J. J., 2006, A&A, 457, 787
Sánchez-Blázquez P., Forbes D. A., Strader J., Brodie J., Proctor R., 2007, MNRAS, 377, 759
Sarzi M. et al., 2006, MNRAS, 366, 1151 (Paper V)
Schulman E., Bregman J. N., Brinks E., Roberts M. S., 1996, AJ, 112, 960
Schweizer F., Seitzer P., 1992, AJ, 104, 1039

Serra P., Trager S. C., 2007, MNRAS, 374, 769
Sérsic J. L., 1968, Atlas de Galaxias Australes. Obs. Astronom., Cordoba
Soria R., Wong D. S., 2006, MNRAS, 372, 1531
Stauffer J. R., 1982, ApJS, 50, 517
Terlevich R., Davies R. L., Faber S. M., Burstein D., 1981, MNRAS, 196, 381
Thomas D., Maraston C., Bender R., 2003, MNRAS, 339, 897
Thomas D., Maraston C., Bender R., Mendes de Oliveira C., 2005, ApJ, 621, 673
Ulvestad J. S., Ho L. C., 2002, ApJ, 581, 925
Vazdekis A., 1999, ApJ, 513, 224
Vazdekis A., Casuso E., Peletier R. F., Beckman J. E., 1996, ApJS, 106, 307
Vollmer B., Huchtmeier W., van Driel W., 2005, A&A, 439, 921
Walcher C. J. et al., 2005, ApJ, 618, 237
Worthey G., Collobert M., 2003, ApJ, 586, 17
Worthey G., Faber S. M., Gonzalez J. J., Burstein D., 1994, ApJS, 94, 687
Young J. S., Xie S., Kenney J. D. P., Rice W. L., 1989, ApJS, 70, 699
Zaritsky D., Kennicutt R. C., Huchra J. P., 1994, ApJ, 420, 87

## APPENDIX A: RADIAL BEHAVIOUR

We briefly investigated the radial variations of the line strength indices and age, metallicity and abundance ratios. From the corresponding maps, we calculated radial profiles of H$\beta$, Fe5015, Mg*b* and age, *Z* and [Mg/Fe] from the one-SSP approach, by averaging the maps on concentric annuli of 0.8 arcsec width. We present these profiles in Figs A1–A3. These plots show that there is a wide variety of radial behaviours among late-type spirals: the line strength indices can be roughly constant in radius (H$\beta$ profile for NGC 488), rising outwards (even very steeply, see e.g. the H$\beta$ profile for NGC 5678), rising inwards (many Fe5015 and Mg*b* profiles). In some cases there are also complicated structures, with 'oscillating' profiles: see, for example, the Fe5015 profile for NGC 864 or 2805 and several others. Some of the 'oscillating' profiles might just reflect the noisy nature of the data for some low surface brightness objects (e.g. the Fe5015 profile for NGC 2805), but others are probably related to real variations of the indices within the galaxy. Despite all this variety, we conclude that in most cases the H$\beta$ absorption strength increases with radius, while Fe5015 and Mg*b* decrease. The fact that the metal lines show most often negative gradients was already known for early-type galaxies, while in the case of H$\beta$ for elliptical galaxies the gradients are consistent with a flat relation with radius, or present a mild positive outwards radial gradient (see Paper VI and references therein).

The stellar population parameters show the same heterogeneous behaviours. Roughly, the age shows most often a complex behaviour with radius, reflecting features recognizable in the maps in

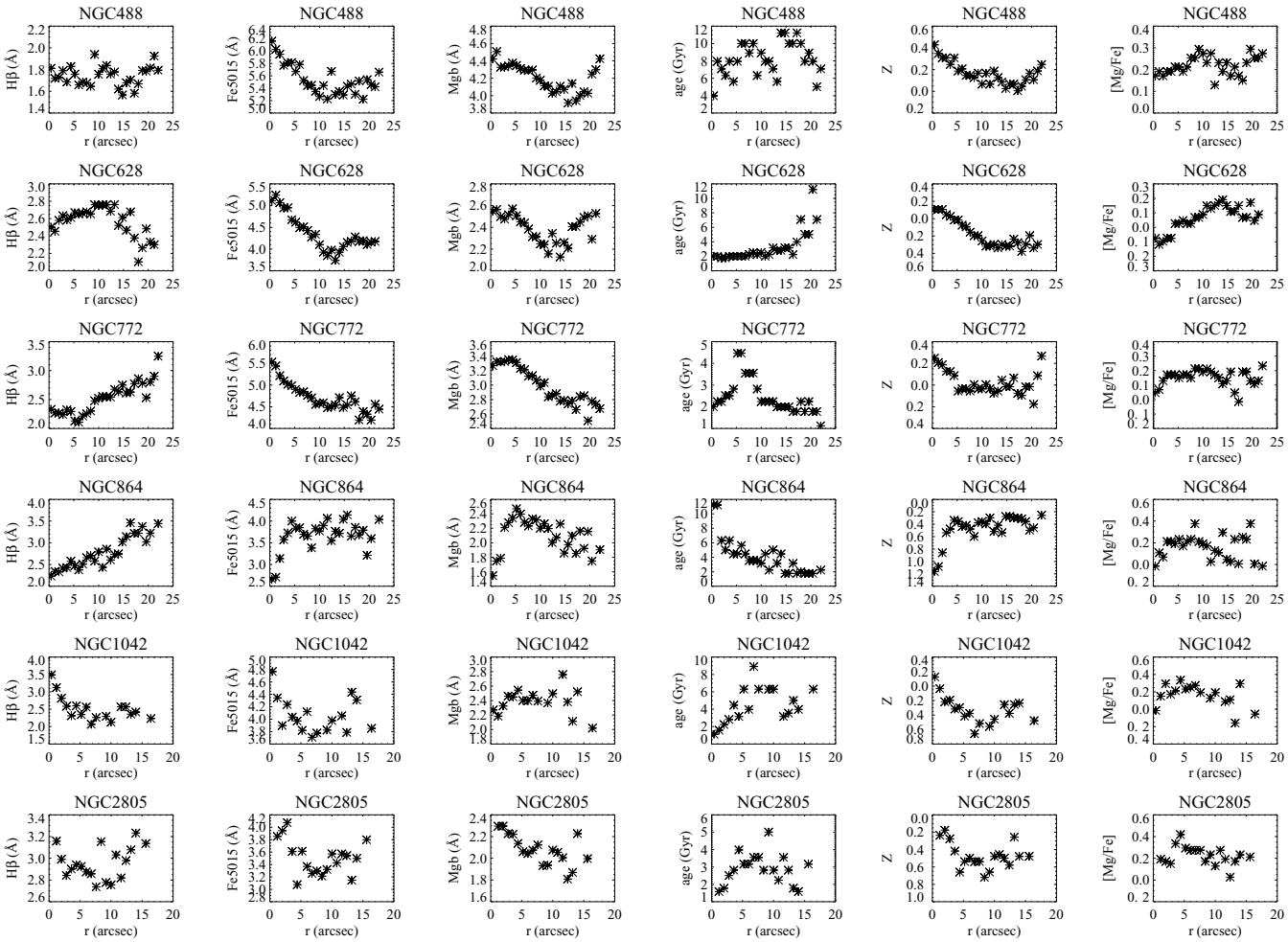


**Figure A1.** Azimuthally averaged radial profiles of the line strength indices H$\beta$, Fe5015, Mg*b* (expressed as equivalent widths and measured in Å) and of the one-SSP analysis parameters age (in Gyr), metallicity and abundance ratio against galactocentric distance (expressed in arcsec); every row presents a different galaxy. See text in Appendix A for a more detailed description. Here we show NGC 488, 628, 772, 864, 1042 and 2805.

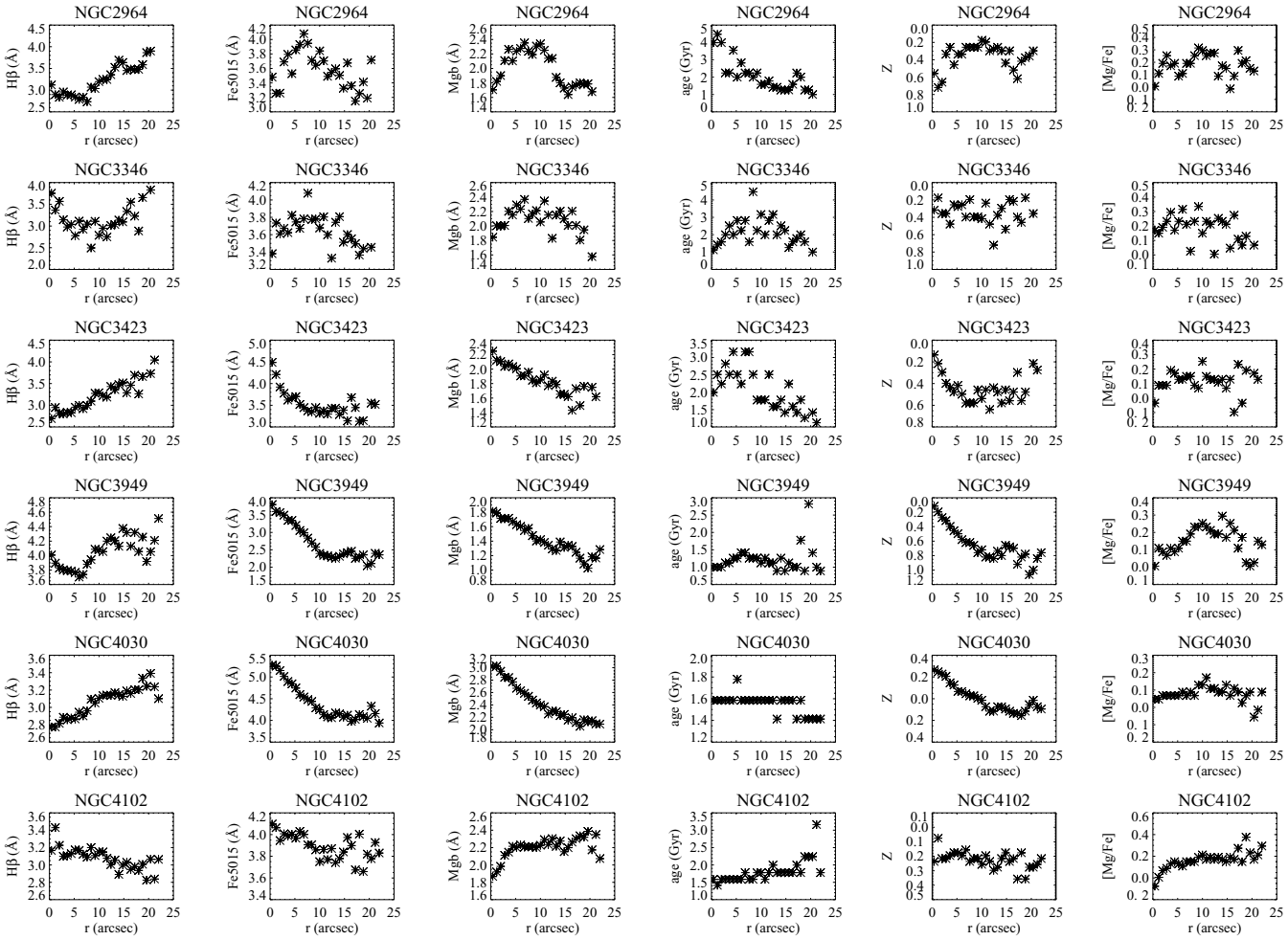


**Figure A2.** Same as Fig. A1 but for NGC 2964, 3346, 3423, 3949, 4030 and 4102.

Figs 6–14, while the metallicity in many cases is decreasing, in agreement with Moorthy & Holtzman (2006), who measure mostly negative metallicity gradients for a sample of S0–Sc galaxies; in the majority of the galaxies, the metallicity profile resembles closely the aspect of the Fe5015 profile. Looking at the abundance ratio profiles in more detail, we see that the central values are usually very close to solar; many of the profiles stay approximately constant with radius, after an initial increase in the bulge-dominated region, which can be very tiny (for a quantitative description of the bulges in these galaxies, we refer the reader to Ganda et al., in preparation). This is also consistent with the findings of Moorthy & Holtzman (2006), that we briefly summarized in Section 5.1: they suggest that the bulges have positive or null gradients in abundance ratio with increasing radius, while the discs have solar abundance ratios. In early-type galaxies, instead, the radial profiles of abundance ratios are rather flat, as found by Kuntschner et al. (in preparation) for the SAURON E/S0 galaxies and by Sánchez-Blázquez et al. (2007) for a sample of 11 E/S0 galaxies; the latter authors do find radial abundance ratio gradients, both positive and negative, but rather shallow.

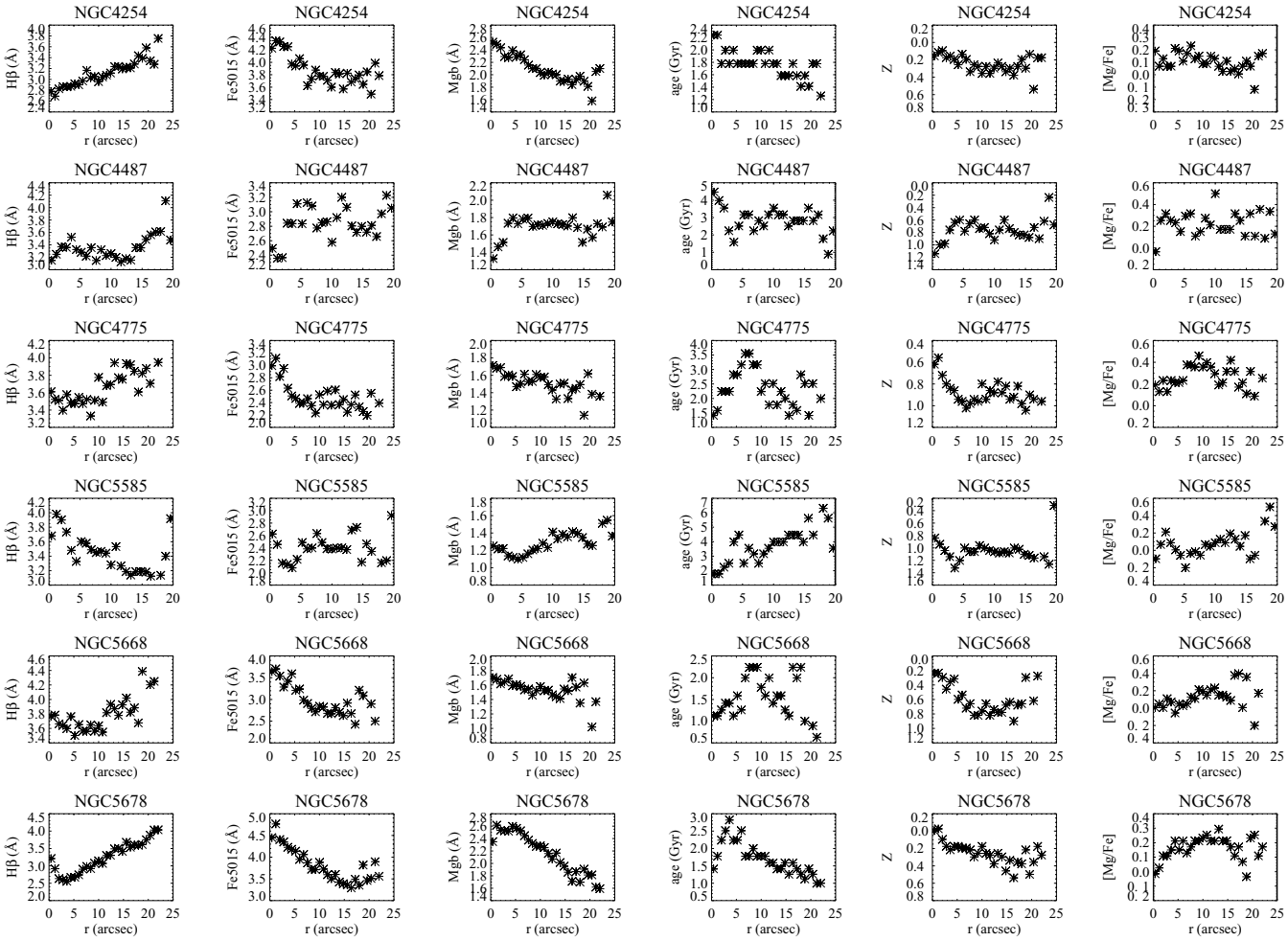


**Figure A3.** Same as Fig. A1 but for NGC 4254, 4487, 4775, 5585, 5668 and 5678.

## APPENDIX B: INDIVIDUAL GALAXIES

### NGC 488

NGC 488 is an unbarred Sb galaxy and it is the most elliptical-like (featureless) object within our sample. NGC 488 has regular stellar and gaseous kinematics, with regular rotation and velocity dispersion smoothly decreasing outwards (Ganda et al. 2006). The line strength maps present high values for Fe5015 and Mg*b* and low values for H$\beta$ over the central regions. As one can note from the values reported in Table 2, this galaxy has the highest Fe5015 and Mg*b* in the sample, and the lowest H$\beta$. The ages are mainly old and the metallicities high. This is indeed the most metal-rich galaxy in the sample (the central metallicity from the one-SSP approach is $\approx$0.49, then it decreases outwards). This galaxy is well described by a one-SSP approach: as shown in Fig. 29 (first column) on the basis of our continuous star formation analysis, NGC 488 is very unlikely to have experienced a constant star formation over time; the observed indices are instead reproduced by a short starburst, approximating an SSP. The time-scale of star formation $\tau$ is short over the whole field. From the profile in Fig. A1, we can see that the [Mg/Fe] profile is approximately constant around the value $\approx$0.2: abundance ratios are slightly supersolar, confirming the fact that this galaxy resembles an elliptical more than the later objects in our sample. Other suggestions in this sense come from the position it occupies in the diagrams in Figs 15, 16 and 19, where it lies in the region occupied by the ellipticals.

### NGC 628

NGC 628, known also as M74, is a grand-design Sc galaxy. Cornett et al. (1994) concluded that the star formation history of NGC 628 varies with galactocentric distance; Natali, Pedichini & Righini (1992) suggested that the galaxy could be seen as an inner and an outer disc characterized by different stellar populations; according to them, the transition between the two regions is located at $\approx$8–10 kpc from the centre. Our observations of NGC 628 are disturbed by the presence of a foreground star which falls close to the centre ($\approx$13 arcsec southern). The stellar kinematics is characterized by slow projected rotation, and velocity dispersion decreasing in the central zones, indicating a cold central region, maybe an inner disc (Ganda et al. 2006). This galaxy is part of the 'control sample' of non-active objects studied by Cid Fernandes et al. (2004), Gonzalez Delgado et al. (2004), Cid Fernandes et al. (2005), who analyse the nuclear spectrum, describing it as a mixture of $10^8-10^9$ yr old and older stars.

As can be seen from the profiles reported in Fig. A1, NGC 628 has ages (one-SSP approach) below 3 Gyr out to $\approx$15 arcsec, and becomes older at larger radius; the features are roughly in agreement with the above mentioned findings of Cid Fernandes

and collaborators; the same trend in age is observed, on the common radial range, also by MacArthur et al. (2007), on the basis of GMOS data independently analysed. The metallicity decreases outwards. The 'bumps' recognizable in the Fe5015, Mg*b* and (but less pronounced) metallicity profiles at ≈13 arcsec from the centre are due to the foreground star. From our continuous star formation analysis, as shown in Fig. 29 (second column), we can state that this galaxy is not described by a constant star formation scenario.

### NGC 772

NGC 772, also called Arp78, is an Sb galaxy characterized by a particularly strong spiral arm; it forms a pair at 3.3 arcmin with the E3 galaxy NGC 770. From the kinematical point of view, NGC 772 is characterized by a clear drop of the stellar velocity dispersion in the central zones, possibly corresponding to an inner disc, as suggested also by the anticorrelation between velocity and the Gauss–Hermite moment h3 (Ganda et al. 2006). In the line strength maps we can clearly see an extended central region with high Fe5015 and Mg*b* and low H$\beta$; indeed, from the central aperture values reported in Table 2 we can see that this galaxy is one of those with the highest metal indices, surpassed only by NGC 488. In the H$\beta$ map it is possible to see, surrounding the central depression, regions with higher values corresponding to the spiral arms. A similar behaviour can be seen in the [O III]/H$\beta$ map presented by Ganda et al. (2006), which shows a structure resembling the spiral pattern. Estimating ages and metallicity by comparison with SSP models, we infer that ages are mainly young–intermediate and the central metallicity is among the highest in our sample. The age and abundance ratio maps display the spiral arms structure as well, like the index maps. Fig. 29 (third column) demonstrates that for this galaxy constant star formation can be ruled out at a high confidence level: high $\tau$ values are never likely. The $\tau$ map shown in Fig. 7 (for age fixed to 10 Gyr in the fitting procedure) presents a spatial structure that partially resembles the H$\beta$ map and the spiral arms pattern. NGC 772 is part of the sample studied in the series of papers by Cid Fernandes et al. (2004); Gonzalez Delgado et al. 2004; Cid Fernandes et al. 2005, who are engaged in a project to examine the stellar populations of low-luminosity active galactic nuclei (AGN). They classify this object as 'young-TO', that is, a transition object between a LINER and an H II nucleus, with weak [O I] $\lambda$6300 emission; they find that the nuclear spectrum is dominated by $10^8-10^9$ yr old stellar populations, with a contribution up to ≈32 per cent from populations younger than $10^7$ yr and a similar contribution also from older stellar populations ($\geqslant 10^9$ yr). Their data probe distances up to several hundred parsecs from the nucleus; they measure in NGC 772 significant radial variations of the stellar populations, with absorption line strengths increasing in the inner 3 arcsec indicating a younger population in the very centre, especially referring to the Ca II K line; the Mg I absorption strength presents instead less prominent variations over the spatial range of their data. Our data cover a different spectral range and a different spatial extension, but we also concluded that the populations in the inner parts have intermediate ages, and that the age (from the one-SSP analysis) increases in the inner ≈5 arcsec (see Fig. A1).

### NGC 864

This is a barred Sc galaxy where a nuclear radio source with the linear size of ≈300 pc has been detected (Ulvestad & Ho 2002); according to Espada et al. (2005) its H I profile is symmetric in velocity but asymmetric in intensity; they also measure large-scale asymmetries in the two-dimensional kinematics, such as a warp. The mentioned asymmetries occur in the outer parts, well beyond the extent of the SAURON field. The asymmetries could have been induced by a past encounter with a companion, passing outside the optical disc but within the H I disc; the companion would have dispersed its stars and dark matter after the merging, consistent with the fact that NGC 864 appears to be remarkably isolated.

Our line strength maps show a very sharp central dip in both Fe5015 and Mg*b*; in the region surrounding the dip, the Fe5015 and Mg*b* values rise. The H$\beta$ absorption also takes on low values over an extended central region; as seen also in Table 2, the indices measured on the central aperture of this galaxy are among the lowest in the sample. From the one-SSP analysis, given the structure of the line strength maps, we derive very low metallicity and old (≈11.22 Gyr) ages for the central aperture.

The analysis of the $\Delta\chi^2$ contours, in the continuous star formation approach, shows that this galaxy is unlikely to have experienced a constant star formation over time (see Fig. 29, fourth column).

### NGC 1042

NGC 1042 is an Scd galaxy forming a pair with NGC 1035 at a separation of 22 arcmin (corresponding to 177 kpc). It has a bright, small nucleus and otherwise low surface brightness. Our line strength maps are quite patchy, due to poor S/N in the data and consequent heavy binning of the spectra. The Mg*b* index takes on low values in the very centre, and higher ones around it. H$\beta$ is high in the centre and low outside it, being flat over most of the map; as can be seen also from the line strength profiles in Fig. A1, the line strength indices stay approximately constant over most of the field, outside a central zone of radius ≈3 arcsec. The age of the stellar populations (one-SSP analysis) reaches a minimum in the centre. The metallicity is everywhere low, and peaks in the centre.

The analysis of the $\Delta\chi^2$ contours for the central aperture, in the continuous star formation approach, shows that this galaxy is not well described by an SSP (see Fig. 29, fifth column). The $\tau$ map for age fixed to 10 Gyr (see Fig. 8) shows a peak in the very centre, corresponding to the peak in the H$\beta$ and to the minimum in the Mg*b* maps.

### NGC 2805

NGC 2805 is an Sd galaxy seen nearly face-on and it is the brightest member of a multiple interacting system containing also NGC 2814 (Sb), NGC 2820 (Sc) at 13 arcmin and IC2458 (I0). H I has been detected (Reakes 1979; Bosma et al. 1980) and there are claims that the outer H I layers are warped (see e.g. Bosma et al. 1980). The galaxy seems to be also optically disturbed, since the spiral arms appear to be broken up into straight segments.

The line strength maps are rather patchy, displaying though a central peak in all three lines. By comparison of our measured indices with SSP models, we can state that the ages are young–intermediate over most of the field; that the metallicity peaks in the centre and that abundance ratios are supersolar.

The analysis of the $\Delta\chi^2$ contours, in the continuous star formation approach, shows that this galaxy is not very well described by an SSP, and that even a constant SFR cannot be excluded at all ages (see Fig. 29, sixth column).

**NGC 2964**

NGC 2964, classified as Sbc, forms a non-interacting pair with the I0 galaxy NGC 2968 at 5.8 arcmin. As discussed by Ganda et al. (2006), the SAURON data reveal that this barred Sbc galaxy hosts an AGN. When we calculate the line strengths, we find that the Mg*b* index assumes low values in an elongated central region, higher values around it, and low values again towards the edges of the field; the Fe5015 index presents a very similar behaviour; the H$\beta$ map has instead an opposite appearance, with an extended inner region with low index values and a surrounding area with higher values; in the very centre a shallow peak might be recognized. These features are recognizable also in the profiles in Fig. A2. We note also that the central region with low Fe5015 and Mg*b* corresponds to the central depression in the emission line [O III]/H$\beta$ map (see fig. 5 in Ganda et al. 2006), possibly indicating ongoing star formation. Converting the line strength maps to age and metallicity via our comparison with the SSP models, we find young–intermediate ages over most of the field, with a peak in the central region, and low metallicity everywhere, with a minimum in the central region, a positive gradient out to ≈5 arcsec, and then a rather constant behaviour out to ≈15 arcsec. From the continuous star formation approach, we cannot exclude at all ages the case of constant star formation, but the $\tau$ map for age fixed to 10 Gyr (in the fitting procedure) presents a large central region with low values, possibly suggesting an ≈5-Gyr-long starburst.

**NGC 3346**

This Scd galaxy is very poorly studied in the literature. Ages of the stellar populations (one-SSP approach) are young–intermediate and metallicity low over most of the field. From the continuous star formation approach, we cannot exclude at all ages the case of constant star formation (see Fig. 30, second column).

**NGC 3423**

This Sbc galaxy is also poorly known. Both the Fe5015 and Mg*b* indices peak in an extended central region and decrease towards the edge of the field; the H$\beta$ map presents opposite behaviour. The $\tau$ map (for age fixed to 10 Gyr in the fitting procedure) displays low values over a large central area, possibly indicating a region where the bulk of star formation happened in a quite short starburst.

**NGC 3949**

NGC 3949 is an Sc galaxy belonging to the Ursa Major cluster. NGC 3949 presents quite regular Fe5015 and Mg*b* line strength maps, peaking in an extended central region and decreasing rather smoothly moving outwards. The H$\beta$ index is low in the central region and higher in the surroundings; interestingly, it reaches a minimum in a zone south of the centre where the emission line ratio [O III]/H$\beta$ is particularly depressed (see relative figure in Ganda et al. 2006). The values measured for the H$\beta$ index are the highest in the sample, as one can see from Table 2 and from Fig. A2. Ages (from the one-SSP approach) are young (≈1.0 Gyr) in the central region, somewhat higher around it and decreasing again towards the edge of the field. The metallicity is everywhere low, and decreasing outwards.

Constant star formation cannot be ruled out; it is likely to characterize the star formation mode over most of the field (see the $\tau$ map for age fixed to 10 Gyr in Fig. 10: $\tau$ assumes high values). Actually, when performing the fit allowing the code to choose among exponentially declining and constant star formation, constant is selected over most of the field.

**NGC 4030**

This Sbc galaxy is characterized by very regular kinematics for both the stellar and gaseous components (Ganda et al. 2006). The line strength maps also have a smooth appearance, with Fe5015 and Mg*b* decreasing at larger radius and H$\beta$ increasing. The H$\beta$ map seems to be asymmetric with respect to the centre, since the western side displays higher values than the eastern one. The stellar populations are young over the whole field and the metallicity, among the highest in our sample (the third after NGC 488 and 772), decreases moving outwards; the abundance ratio is approximately solar. The $\tau$ map for age fixed to 10 Gyr in Fig. 11 shows a large central depression. The analysis of the $\Delta\chi^2$ contours, in the continuous star formation approach, shows that this galaxy is probably not very well described by an SSP, nor by a constant SFR.

**NGC 4102**

NGC 4102 is an Sb galaxy, classified as a LINER in the NED data base; it is known to be a powerful far-infrared (FIR) galaxy (Young et al. 1989) and also to have a strong nuclear radio source (Condon et al. 1982). Devereux (1989) classified it as one of the most powerful nearby starburst galaxies. The signs of activity are detectable also in the SAURON data: as noted by Ganda et al. (2006), the [O III] maps trace the outflowing gas, with a region of very high gas velocity dispersion corresponding also to high values in the [O III]/H$\beta$ line ratio map, as expected for an active object. In that same region, we observe double-peaked line profiles for the [O III] emission lines, pointing towards the presence of different components in the emitting material. As for the line strength indices, Mg*b* is low in an inner region, increases around it, and decreases again in the outer parts. The Fe5015 map is instead more centrally concentrated. The map of H$\beta$ absorption looks more complex and not symmetric. Ages (from our one-SSP analysis) are young all over the field and metallicity is low. Neither in the line strength nor in the age and metallicity map is there a clear connection with the mentioned region of activity. On the basis of our continuous star formation analysis, this galaxy is probably not very well described by an SSP.

**NGC 4254**

Also known as M99, NGC 4254 is a bright Sc galaxy located on the periphery of the Virgo cluster, at a projected distance of $3^\circ.7$ (≈1 Mpc) from the centre of the cluster. Its optical appearance is dominated by a peculiar one-arm structure: the arms to the northwest are much less defined than the southern arm. This kind of spiral structure could be related to an external driving mechanism, but for NGC 4254 there are no close companions. Phookun, Vogel & Mundy (1993) carried out deep H I observations of NGC 4254, detecting non-disc H I clouds, with velocities not following the disc velocity pattern and an extended low surface density tail northwest of the galaxy; they interpreted these observational results as infall of a disintegrating gas cloud. They also noted that there is an hole in the H I emission at the centre of the galaxy, with a diameter of ≈3 kpc. Vollmer, Huchtmeier & van Driel (2005) propose instead a scenario where NGC 4254 had a close and rapid encounter with another massive galaxy when entering the Virgo cluster: the tidal interaction

caused the one-arm structure and the H I distribution and kinematics is due to ram pressure stripping. Recently, Soria & Wong (2006) studied the X-ray properties of M99, noticing that a phenomenon often associated with tidal interactions and active star formation – both documented – is the presence of ultraluminous X-ray sources (ULXs). The X-ray emission appears approximately uniformly diffused across the inner ≈5 kpc from the nucleus. They do find a ULX, amongst the brightest observed, located at ≈8 kpc southeast of the nucleus, close to the position where a large H I cloud seems to join the gas disc. From observations of the radial velocities, they suggest that the cloud is falling on to the galactic disc and try to build a link between this collisional event and the formation of the bright ULX. Our data cover a much smaller spatial extent than the mentioned observations, therefore a comparison is not possible; within our field, both the Fe5015 and Mg*b* maps show a regular structure with a central concentration; at the northern edge of the field, both Fe5015 and Mg*b* seem to increase again; the H$\beta$ map has opposite behaviour, presenting a central depression. The ages (from our one-SSP approach) are generally young and the metallicity, quite low everywhere, decreases slightly moving outwards and shows the same enhancement at the northern edge of the field that we noted for the Fe5015 and Mg*b* line strength. The $\tau$ map (see Fig. 12) shows a central depression. The analysis of the $\Delta\chi^2$ contours, in the continuous star formation approach, shows that NGC 4254 is probably not very well described by an SSP, nor by a constant SFR.

### NGC 4487

This Scd galaxy forms a pair with the Scd galaxy NGC 4504, at a separation of 35 arcmin (corresponding to ≈165 kpc). The Fe5015 and Mg*b* maps seem to be low in the very centre and higher outside it; from the profiles in Fig. A3 one can see that outside the inner circle of ≈3 arcsec radius, the line strengths keep an approximately constant value, out to ≈13 arcsec. Ages (one-SSP approach) are intermediate–young and metallicities very low, with, respectively, a maximum and a minimum in the centre. Constant star formation cannot be ruled out.

### NGC 4775

NGC 4775 is an Sd galaxy, for which very little is known from previous studies. The metal lines (Fe5015 and Mg*b*) seem to be centrally concentrated, while H$\beta$ is low over an extended central area, and higher in the surrounding region. The maps are not symmetric with respect to the centre. The galaxy is young in the nucleus and has older ages in an annular (extended) region around the centre; the metal content is everywhere low, and peaks in the centre. Constant star formation cannot be ruled out, and is selected over a large part of the field when allowing one to choose among constant and exponentially declining star formation.

### NGC 5585

NGC 5585 is a barred Sd galaxy; together with NGC 5204 (Sm), NGC 5474 (Scd), NGC 5477 (Sm), HoIV (Im) and M101 (Scd) it forms the M101 group. The Fe5015 and Mg*b* indices assume values among the lowest in the sample; H$\beta$ has instead a value among the highest ones (see Table 2). The metallicity retrieved from the one-SSP analysis is everywhere very low. In the continuous star formation approach, constant star formation cannot be ruled out; indeed, when allowing to choose among exponentially declining and constant star formation, in the $\chi^2$ minimization, for age fixed to 10 Gyr the constant star formation is selected (for the central aperture).

### NGC 5668

NGC 5668 is another Sd galaxy, which has a high rate of star formation, as indicated by its large FIR and H$\alpha$ luminosities (Schulman et al. 1996, and references therein). The metal lines (Fe5015 and Mg*b*) appear to be centrally concentrated, while H$\beta$ has a more complex appearance. The stellar populations are young and metal-poor all over the field; the age rises out to ≈8 arcsec and then decreases (see Fig. 14 for a full view of the spatial structure of the age map and Fig. A3 for the azimuthally averaged profiles). Constant star formation cannot be ruled out at all ages, and is selected over a large part of the field when allowing one to choose among constant and exponentially declining star formation.

### NGC 5678

This is a barred and very dusty Sb galaxy. Fe5015 and Mg*b* have a quite regular and centrally concentrated appearance; H$\beta$ is depressed in the inner region and increases in an annulus-like structure around it. In the very centre H$\beta$ has a local maximum, as shown also in the azimuthally averaged profile in Fig. A3. Ages (one-SSP approach) are young over most of the field and the metallicity, rather low everywhere, decreases moving outwards. The $\tau$ map at age fixed to 10 Gyr (see Fig. 14) shows a large central depression. The analysis of the $\Delta\chi^2$ contours shows that NGC 5678 is probably not very well described by an SSP, nor by a constant SFR. Like NGC 628 and 772, this galaxy is part of the sample studied in the Cid Fernandes et al. papers (Cid Fernandes et al. 2004; Gonzalez Delgado et al. 2004; Cid Fernandes et al. 2005); following their classification, it is a 'young-TO' galaxy, with weak emission in the [O I] $\lambda$6300 line; according to those authors, the nuclear spectrum is heavily dominated by $10^8-10^9$ yr old stellar populations, with negligible contribution from stars younger than $10^7$ yr. They detect radial variations of the absorption indices, particularly in the Ca II K line, but less clearly evident than in the case of NGC 772.

This paper has been typeset from a TEX/LATEX file prepared by the author.